Carbon 123 (2017) 318–333

Contents lists available at ScienceDirect

Carbon

journal homepage: www.elsevier.com/locate/carbon

High-performance activated carbon from polyaniline for capacitive deionization

Rafael L. Zornitta [a, *], Francisco J. García-Mateos [b], Julio J. Lado [a, c], José Rodríguez-Mirasol [b], Tomás Cordero [b], Peter Hammer [d], Luis A.M. Ruotolo [a, **]

[a] Department of Chemical Engineering, Federal University of São Carlos, Rod. Washington Luiz km 235, 13565-905, São Carlos, SP, Brazil
[b] Department of Chemical Engineering, Andalucía Tech, University of Málaga, Campus de Teatinos s/n, 29010, Málaga, Spain
[c] Madrid Institute for Advanced Studies, IMDEA Energy, (Electrochemical Processes Unit), 28933, Móstoles, Madrid, Spain
[d] Institute of Chemistry, São Paulo State University – UNESP, Rua Prof. Francisco Degni, s/n, 14800-900 Araraquara, SP, Brazil

ARTICLE INFO

Article history:
Received 28 March 2017
Received in revised form
10 July 2017
Accepted 21 July 2017
Available online 24 July 2017

ABSTRACT

Activated carbons prepared using polyaniline (PAni), a N-containing precursor, doped with different anions were successfully employed in this work as electrode materials for capacitive deionization. The aim of this research was to investigate the effect of chloride (Cl^-), *p*-toluenesulfonate (PTS^-), dodecylbenze-sulfonate (DBS^-) and polystirenesulfonate (PSS^-) as PAni dopants on the textural and electrochemical properties of PAni activate carbon (PAC) and evaluate their performance for desalination. It was demonstrated that textural PAC properties such as microporosity could be properly tuned, resulting in a suitable proportion of micro- and mesoporosity by using different doping anions. Furthermore, it was observed that the higher the oxygen content the higher the electrode hidrophilicity due to introduction of surface polar groups, as identified by XPS. These groups were found to be the most important variable influencing on the PAC electrosorption capacity and energy efficiency. The highest specific adsorption capacity (14.9 mg g^{-1}), along with the lowest specific energy consumption, was obtained using the PTS-doped PAC electrode. Considering its high capacity, low-cost and ease of synthesis, PAC/PTS seems to be a promising electrode for CDI.

1. Introduction

Water scarcity as result of population growth and industrialization has become one of the major issues of the 21st century. Despite the large reserves of water still available on earth (e.g. seawater and groundwater), great part of this water does not meet quality standards for human consumption mainly due to the high concentration of salts. To make water drinkable, reverse osmosis (RO), electrodialysis (ED), and multi-effect distillation (MFD) can be employed for water desalination, although these technologies demand high energy consumption in large-scale applications [1,2]. In this context, CDI has emerged in the last few years as a low-cost technology that can be used to remove ions from brackish water (~10,000 mg L^{-1}), but consuming less energy than its main competitor, the RO [2]. CDI is based on the concept of charge storage in the electric double layer (EDL) developed when ions are attracted to a pair of porous carbon electrodes when an external voltage is applied. The low energy consumption of CDI comes from the low voltage needed for the electrosorption process (typically 1.0–1.4 V) and the low required pressure when compared to RO [3–5]. After electrode saturation, the regeneration of the electrodes is achieved by short-circuiting the cell [4,6]. Another possibility is to invert the cell potential repelling the electrosorbed ions, thus reducing the time needed for electrode regeneration (Fig. S1) [5].

Despite the advantages presented by CDI relative to other well-established technologies like RO and ED, there are still challenging issues, such as electrode material, to be overcome in order to make this technology feasible for large-scale applications. The electrode material for CDI must have fast electrosorption kinetics and high adsorption capacity. A good candidate for electrode material to be used for CDI must have high specific surface area (SSA) available for electrosorption, high conductivity, good wettability, fast response to polarization, and chemical stability [7]. Carbon materials fit most

* Corresponding author.
** Corresponding author.
E-mail addresses: rafael_rlzs@hotmail.com (R.L. Zornitta), pluis@ufscar.br (L.A.M. Ruotolo).

http://dx.doi.org/10.1016/j.carbon.2017.07.071
0008-6223/

of these requirements and have been intensively used as CDI electrodes, e.g., carbon aerogels [3,8,9], mesoporous activated carbon [4,10], microporous activated carbon [11], carbon felts [12], carbon fibers [13], carbon nanotubes [14,15] and their modification using oxides [16,17] and conducting polymers [18,19]. Although there are many studies related to electrode materials for symmetrical membraneless CDI, the carbons showing the best performance, such as nitrogen doped graphene, are still too expensive and in many cases their preparations are not environmental friendly [20].

Recently, nitrogen-doped activated carbons (N-doped AC) have been reported to enhance CDI electrode performance [21–24] mainly due to the (i) introduction of defects and distortion in the carbon matrix, facilitating the ion access to the surface area and increasing charge accumulation, (ii) enhancement of charge density due to the presence of nitrogen, which facilitates the charge-transfer process [24,25], and (iii) introduction of surface groups responsible for pseudocapacitance [21]. CDI materials reported to exhibit the highest specific adsorption capacity (SAC) are N-doped graphene (21.9 mg g^{-1}) [21], N-doped graphene sponge (21 mg g^{-1}) [25], and N-doped cotton-derived carbon sponge (16.1 mg g^{-1}) [24]. The most common approach to introduce N-groups into the carbon structure is the post-treatment with ammonia at high temperatures. However, this technique leads to a low nitrogen content and poor thermal stability [26]. Moreover, this process could become too expensive considering the precursor preparation followed by the activation with ammonia.

Nitrogen-containing precursors such as glucosamine hydrochloride [23], polyacrylonitrile [27], PAni [28–30] and polypyrrole [31] have become a low-cost alternative to obtain N-doped AC dispensing the post-treatment. Among these materials, PAni find applications in different fields such as supercapacitors [32], cation exchange [33], and as additive to improve AC capacitance in CDI [19,34]. PAni presents high nitrogen-content (~15 wt%), it is inexpensive, easily synthetized, and has a structure similar to graphite, which could facilitate the introduction of nitrogen-containing active sites inside the carbon matrix at high temperatures [30,35]. Furthermore, the PAni properties can be easily customized by varying the doping anion during the polymerization process [36]. The use of PAni as AC precursor has already been reported for different applications such as adsorption [37], supercapacitors [29,30,36,38–45], electrocatalysts [35,41], and batteries [45]; however, to the best of our knowledge, PAC has never been used for CDI applications.

PAC has been considered a promising material for electrochemical applications due to its distinguished structural and textural characteristics. Recent studies have shown that depending on the precursor synthesis and activation method, PAC presents extremely high SSA [37,44,45], high mesopore volume [40], high capacitance [29,43], good wettability [43], and long-term stability [29,30]. The presence of quaternary nitrogen in the carbon matrix can enhance the charge-transfer, thus improving the CDI electrode conductivity [24,25]. Moreover, the presence of pyridine- and pyrrole-like nitrogen groups is recognized as being responsible to create pseudocapacitance [21] and also to improve carbon wettability due to the redox reaction with water according to Equation (1) [25,46].

$$-CH = NH + 2e^- + H_2O \rightleftharpoons -CH - NHOH$$

In this scenario, the application of PAC as CDI electrodes seems to be promising and was the aim of this investigation. To the best of our knowledge, the use of PAC for CDI using PAni doped with different anions is reported for the first time. PAni was used as N-containing precursor to obtain a N-doped AC. Furthermore, the effect of the large (dodecylbenzene-sulfonate, DBS^-, and polystirenesulfonate, PSS^-) and small dopant anions (Cl^- and *p*-toluenesulfonate, PTS^-) on the textural properties of the obtained PAC was compared.

In order to understand the effect of different anions on the PAC electrode performance for desalination, PACs were characterized regarding to their SSA, pore size distribution (PSD), morphology, surface functional groups, electrochemical capacitance and charge-transfer resistance. The desalination performance was evaluated in terms of electrosorption kinetics, SAC, charge efficiency and specific energy consumption. The results confirmed the great potential of this novel approach to explore the properties of PAni to obtain tailorable N-doped activated carbons for CDI electrodes.

2. Experimental

2.1. Materials

The monomer aniline (99% Sigma-Aldrich) was distillated prior to use for polymerization and maintained in amber bottle at low temperatures (<3 °C) to prevent oxidation. Anion sources used as counter ions for polyaniline were hydrochloric acid (HCl, 36.5–38%, J.T. Baker), *p*-toluenesulfonic acid monohydrate (HPTS, ≥98.5%, Sigma-Aldrich), sodium dodecylbenzene-sulfonate (NaDBS, Sigma-Aldrich) and poly(4-styrenesulfonic acid) (HPSS, 18 wt % solution in water, Sigma-Aldrich). The oxidant used for polymerization was ammonium persulfate (98%, Sigma-Aldrich). Polyvinylidene fluoride (PVDF, Sigma Aldrich) and n-methylpyrrolidone (NMP, 99.5%, Synth) were used as binder and solvent, respectively, for electrode preparation. Commercial activated carbon (CAC) YP-50F was purchased from Kuraray Corp., Japan.

2.2. Polyaniline synthesis

PAni was chemically synthesized using the optimized conditions adapted from Jelmi et al. [47] Briefly, 10 mL of aniline (0.21 mol L^{-1}) was added at low temperature (~3 °C) and constant stirring to 500 mL solution containing 0.30 mol L^{-1} of the doping compounds (HCl, HPTS, NaDBS and HPSS). The polymerization started adding 85.9 mL of the oxidant solution ($(NH_4)_2S_2O_8$ 1.0 mol L^{-1}), dropped slowly into the monomer solution. The mixture was left to react for 24 h under stirring. After polymerization, the precipitated PAni doped with Cl^- and PTS^- were filtered, washed with acid solution (HCl and HPTS, respectively) and dried in oven at 60 °C for 24 h [43]. Regarding to PAni doped with DBS^-, 750 mL of acetone (99.5%, Synth) was added to the polymerization solution to precipitate the polymer particles, followed by filtration and washing with plenty of water and dried in oven at 60 °C for 24 h [48,49]. The particles of PAni doped with PSS^- were separated by leaving the polymerization solution in an oven for 24 h at 60 °C to evaporate the solvent [50]. The samples of PAni doped with the different anions were referred as PAni/Cl, PAni/PTS, PAni/DBS and PAni/PSS.

2.3. Polyaniline carbonization and activation

PAni was activated according to the procedure adapted from Yan et al. [29]. In this procedure, PAni was firstly carbonized in a tubular furnace (Thermo Scientific Lindberg Blue M) at 850 °C at a heating rate of 10 °C min^{-1} for 2 h under N_2 atmosphere (150 mL min^{-1}). After carbonization, the samples were activated with KOH in a proportion of 1:4 (polymer:KOH, w/w) followed by heating at 850 °C for 1.5 h using the same heating rate and N_2 flow conditions of the carbonization process. The ratio 1:4 (w/w) of carbonized carbon to KOH was chosen based on previous studies reporting an

increase of 41% of the SSA when the activation agent KOH was increased from 1:2 to 1:4 [43].

After carbonization, the activated carbon was washed with HCl 0.5 M and warm water until constant pH and then dried at 105 °C for 24 h. The samples were referred as PAC followed by the doping source of the PAni precursor: PAC/Cl, PAC/PTS, PAC/DBS and PAC/PSS.

2.4. Preparation of the CDI electrodes

Carbon electrodes were prepared by mixing 10 wt% of PVDF previously dissolved in NMP and 90 wt% of activated carbon. The slurry was kneaded and poured into a mold containing a graphite substrate. The mold was then placed into an oven at 80 °C for 12 h to remove all the solvent and form the carbon film [5]. The mass of the active material in the electrodes used in the desalination experiments was ~0.64 g.

2.5. Material characterization

Doped PAni was characterized by Fourier transform infrared spectroscopy FTIR (Bruker Vertex 70 spectrophotometer) using the KBr pellet technique. Activated carbon morphology was analyzed by scanning electron microscope (SEM, JEOL JSM-840) using high voltages (20–25 kV) and depositing a gold layer to increase conductivity. SSA and PSD were investigated through N_2 adsorption/desorption at −196 °C using an Omnisorp 100cx (Coulter). The samples were prior outgassed for at least 8 h at 150 °C. The volume of micropores and the SSA were calculated from the N_2 isotherm using t-plot method and the Brunauer-Emmett-Teller (BET) equation, respectively. The mesopore volume was determined by the difference between the total pore volume of N_2 adsorbed at $P/P_0 = 0.95$ and the micropore volume. The PSD between 1 and 20 nm was calculated using the density functional theory (DFT) method. X-Ray photoelectron spectroscopy analysis (XPS) was performed using a 5700C model Physical Electronics apparatus with Mg Kα radiation (1253.6 eV). This technique was used for a quantitative analysis and determination of the chemical bonding structure of the PAC samples. The spectra were fitted without placing constraints using multiple Voigt profiles using the CasaXPS software. The ultimate analysis of the samples were performed in a Leco CHNS-932 system, being the oxygen content calculated by difference.

2.6. Electrochemical characterization

Cyclic voltammetry (CV), galvanostatic charge-discharge, and electrochemical impedance spectroscopy (EIS) were performed in NaCl 0.2 mol L^{-1} using a three-electrode cell with carbon electrodes as working (2.5 cm × 2.5 cm) and counter electrode (2.5 cm × 3.0 cm). The reference electrode was Ag/AgCl in saturated KCl. A potentiostat Autolab PGStat 204 was used in all measurements.

CV was carried out at different scan-rates (ν): 1, 5, 10, 50, and 100 mV s^{-1}, in a potential window between −0.2 V and 0.5 V, which was previously determined to prevent redox reactions. The specific capacitance (C_S) and the total specific capacitance (C_{CV}) of the electrode (F g^{-1}), was calculated using Equations (1) and (2), respectively, where I is the current, m is the mass of the working electrode (g) and E_1 and E_2 are the low and high values of the potential window.

$$C_S = \frac{I}{\nu m} \tag{1}$$

$$C_{CV} = \frac{\int_{E_1}^{E_2} IdV}{\nu m(E_2 - E_1)} \tag{2}$$

The galvanostatic charge-discharge experiments were carried out at ± 0.4 mA cm^{-2}. In this case, the specific capacitance (C_{CD}) was calculated from the slope of the discharge curve using Equation (3), where I_d (A) is the discharge current, Δt (s) is the discharging time, and ΔU is the potential drop during discharging (excluding IR drop). The inferior and superior electrode potential cutoffs used in these experiments were 0 V and 0.6 V, respectively.

$$C_{CD} = \frac{I_d \Delta t}{m \Delta U} \tag{3}$$

EIS measurements were carried out in the frequency range between 1 mHz and 100 kHz applying a potential of 0.0 V and an AC amplitude of 10 mV. Specific capacitance obtained from EIS (C_{EIS}) was calculated using Equation (4), where ω is the angular frequency and Z'' is the imaginary part of the impedance spectrum. The fitting for the equivalent circuit was performed using the Metrohm Autolab NOVA v1.11 software.

$$C_{EIS} = \frac{1}{m|\omega Z''|} \tag{4}$$

2.7. Electrosorption experiments

The CDI experiments were used to evaluate the desalination performance in a batch experimental system. A detailed description of the CDI cell can be found in our previous work [5]. Briefly, the electrosorption unit cell consisted of two acrylic plates where carbon electrodes with dimensions of 10 cm × 5 cm were placed on titanium sheets used as current collectors. Two plastic meshes placed between the carbon electrodes provided a gap of 1.8 mm necessary for ensuring the electrolyte flow and preventing short circuit. Rubber gaskets sealed up the cell and all the components were assembled by nuts and bolts.

During desalination, a volume of 25 mL of NaCl 600 mg L^{-1} solution was pumped through the CDI cell using a peristaltic pump (Masterflex L/S Cole-Parmer) at a constant flow-rate of 26 mL min^{-1}. A potentiostat Autolab PGStat 204 supplied the constant cell potential (1.2 V or 1.4 V) during electrosorption and 0 V during desorption. The solution conductivity was measured online at the exit of the cell and it was recorded every 30 s using a conductivity meter (Mettler Toledo SevenCompact Conductivity). The conductivity was then converted to salt concentration using a linear relationship obtained prior to the experiment. Each electrosorption/desorption experiment was performed until no apparent conductivity variation was observed.

Salt adsorption capacity (SAC), charge efficiency (Q_E) and specific energy consumption (η) were calculated using Equations (5)–(7), respectively, and used to evaluate the performance of the electrode in the desalination process.

$$SAC = \frac{(C_0 - C_t)\, V}{m_E} \tag{5}$$

$$Q_E = 100\frac{zFV\Delta C}{\int I_e d} \quad (6)$$

$$\eta = \frac{E_{cell}\int Idt}{m_{rem}} \quad (7)$$

In these Equations, C_0 is the initial salt concentration (mg L^{-1}), C_t (mg L^{-1}) is the salt concentration at time t, V is the volume of electrolyte (L), m_E is the mass of active material in both electrodes, z is the ion charge, F is the Faraday constant (96,485 C mol^{-1}), E_{cell} is the cell voltage during electrosorption (V), m_{rem} is the mass of ions removed. The current (I_e) in Equation (6) is the effective current used for electrosorption (subtracting the leakage current) while the current (I) in Equation (7) is the total current applied to the cell.

3. Results and discussion

3.1. Polymerization and activation

Table S1shows the polymerization yield (Y_{PAni}) calculated from the ratio of polyaniline/aniline (wt./vol.) for the solutions containing the different anions. The highest yield was achieved using PSS^- followed by DBS^- and PTS^-. This result can be explained by the high molecular weight of PSS^- (~75,000 g mol^{-1}), followed by DBS^- (348.5 g mol^{-1}) and PTS^- (172.2 g mol^{-1}). As the size of the anion gets smaller, the PAni final mass also decreases, reaching the lowest value for PAni/Cl. The polymerization process was adapted from the best yield conditions obtained by Jelmy et al. [47], although the doping anion used in their work was the methanesulfonate. Nevertheless, it was possible to observe a high Y_{PAni} considering that for most of the experiments the final mass of PAni was close or even higher than the mass of aniline used for polymerization. For comparison, John et al. [51] synthesized PAni/PTS and obtained a Y_{PAni} of 91.4% with respect to aniline which is fairly close to the 82% achieved is this work.

Another way to estimate Y_{PAni} is to consider the ratio of the mass of the conducting polymer and the total mass of aniline plus the doping anion. In this case, the PAni/DBS yield only 26.7%, which is much lower than the 92.3% obtained by Shreepathi [48], but this author used acidic DBS instead of the sodium salt used in this work. A possible explanation for the lower Y_{PAni} observed for PAni/DBS might be the high pH of the salt solution. The lower the pH the more protonated the PAni [52] and, consequently, there will be more doping sites for DBS^-. Therefore, it can be concluded that Y_{PAni} can be further optimized using different polymerization conditions.

After polymerization, the PAni powder was first carbonized and in a second step activated according to the methodology adapted from Yan et al. [29], which describes the preparation of high SSA PAC/Cl for high performance supercapacitor. Table S2 displays the mass yield for the different materials obtained after carbonization (Y_C), activation (Y_{AC}), and the overall yield (Y_O). It is interesting to notice that the sequence of Y_O for carbonization and activation is the opposite of the polymerization yield (Table S1). This could suggest that most part of the doping anion had been released during the carbonization or activation processes; therefore, the highest mass loss was obtained after the activation process of the PAni doped with the highest molar weight anion.

3.2. Characterizations

3.2.1. FTIR

Prior carbonization and activation, FTIR was performed to investigate if PAni polymers have been successful doped and also to understand the bonding of PAni with the different anions.

Fig. 1(a) shows the FTIR spectra. Despite of some similarity, each spectrum showed typical peaks related to the dopant structure. In all cases, PAni presented N–H stretching at ~3440 cm^{-1}, N–H bending in the range of 1560–1640 cm^{-1}, C–C stretching at ~1100 cm^{-1}, C–C twisting at 1235 cm^{-1}, C–N stretching of the benzenoid at 1300 cm^{-1} and 1407 cm^{-1}, C═C stretching of the benzenoid ring in the range of 1477–1490 cm^{-1}, C═C stretching of the quinoid ring in the range of 1585–1599 cm^{-1} and the N–H out-of-place deformation at 800 cm^{-1} [51–54]. The small peak observed between 735 and 758 cm^{-1} for PAni/Cl indicates the presence of N–Cl [55,56], confirming the PAni was doped by Cl^-. For PAni/PTS, PAni/DBS and PAni/PSS the peaks between 513 and 560 cm^{-1} and 1130-1140 cm^{-1} indicate the presence of SO_3^-, also confirming the doping [51,53,54].

Fig. 1(a–d) confirmed the PAni doping by different anions after polymerization. During oxidation, the nitrogen atoms between quinonoid and benzenoid rings are protonated and a positive charge emerged in the polymer backbone, which is compensated by the negative charge of the anion, characterizing the polymer doping. Depending on the polymerization conditions, PAni may be more or less oxidized, varying from leucoemeraldine (fully reduced) to pernigraniline (fully oxidized). Nevertheless, the emeraldine state (approximately 50% oxidized) is commonly obtained for the most of the synthesis conditions reported in literature [48]. The presence of quinonoid and benzenoid rings determined by FTIR is an evidence that the polymer has oxidized and reduced units, thus indicating an intermediate oxidation state between leucoemeraldine and pernigraniline. The oxidation state probably plays an important role on the polymerization yield because the doping level directly depends on the oxidation state. The higher the oxidation state the higher the doping. Moreover, the anion volume may cause steric hindrance and have influence on the doping process [48].

3.2.2. Morphology

The different morphologies obtained for doped PAni after carbonization and activation are shown in Fig. 2. The size and shape of the AC particles varied according to the dopant employed. The PAC/Cl particles (Fig. 2(a)) were smaller and presented an irregular granular shape, similar to the morphology reported by Yan et al. [29]. The morphology of PAC/Cl retains the original morphology of the precursor PAni/Cl [29]. PAC/PTS and PAC/DBS (Fig. 2(b) and (c)) particles were larger and smoother than those of PAC/Cl, presenting also small cavities and sponge-like shape. PAC/PSS (Fig. 2(d)) also presents smooth surface, but unlike PAC/PTS and PAC/DBS, no cavities were observed. Similarly to PAC/Cl, the PAC/PSS also retains the same precursor morphology after carbonization and activation [37]. It is important to point out that the PAni morphology strongly depends on the method and solvent used for the synthesis [57] and the PAC characteristics depends directly on its precursor [29].

3.2.3. Elemental analysis and surface groups

Elemental analysis and surface composition near the surface region (<5 nm) obtained by quantitative XPS analysis, are presented in Table 1, including as reference one sample prepared without KOH activation, referred to PC/Cl. It can be observed that the PACs are mainly composed by carbon and oxygen. As expected, the oxygen content increased after activation with KOH since the hydroxyl ion present in KOH is a strong oxidant [44].

The deconvoluted XPS core-level spectra of C 1s, shown in Fig. 3, indicate that about 70% of the carbon is present in form of aromatic structures (component at 284.4 eV, ~60% of the peak area) and aliphatic C–H groups at 285.3 eV (~10%). The introduction of

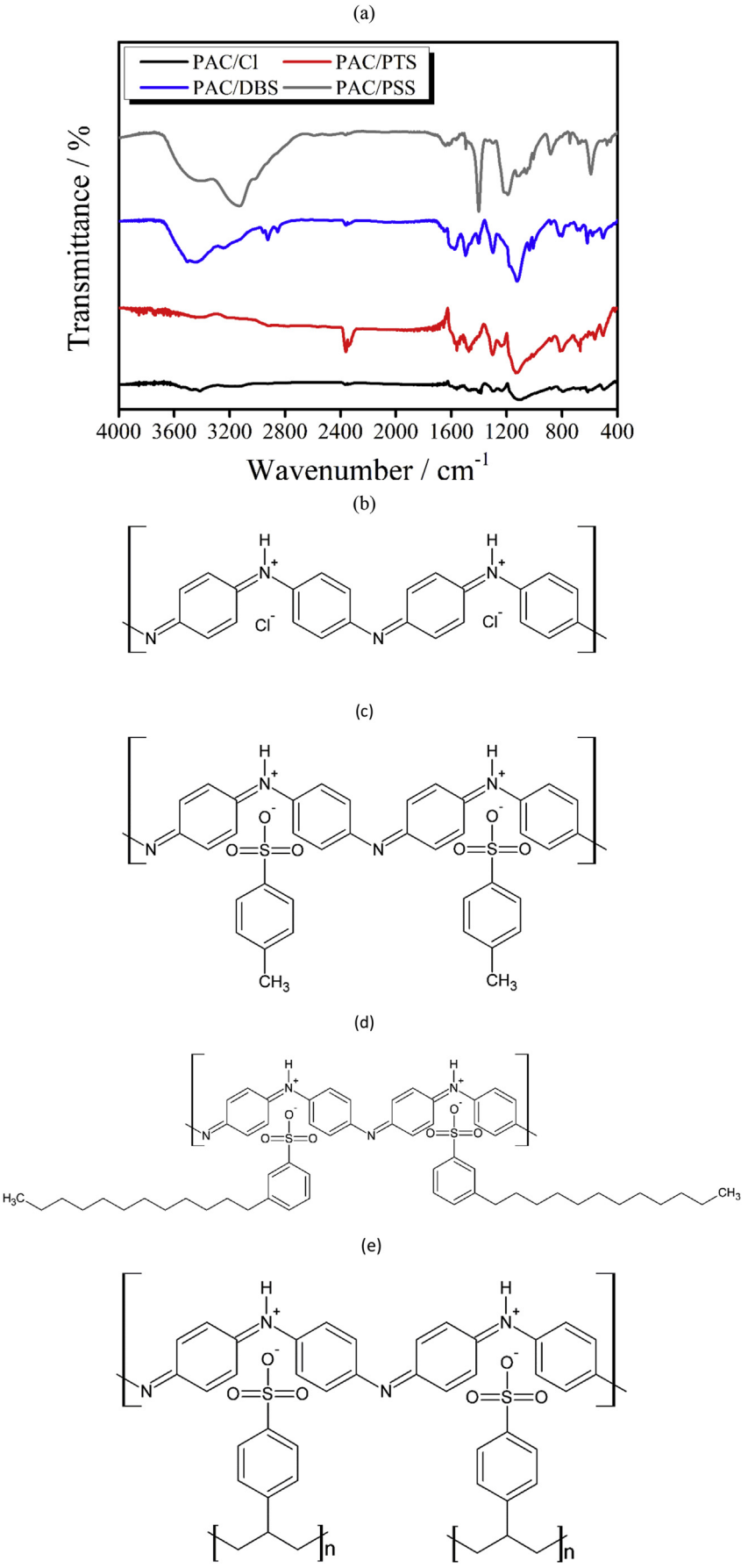

Fig. 1. Infrared spectra of PAni doped with different anions (a) and schematic representation of the anion doping: (b) Cl^{-}, (c) PTS^{-}, (d) DBS^{-}, and (e) PSS^{-}. (A colour version of this figure can be viewed online.)

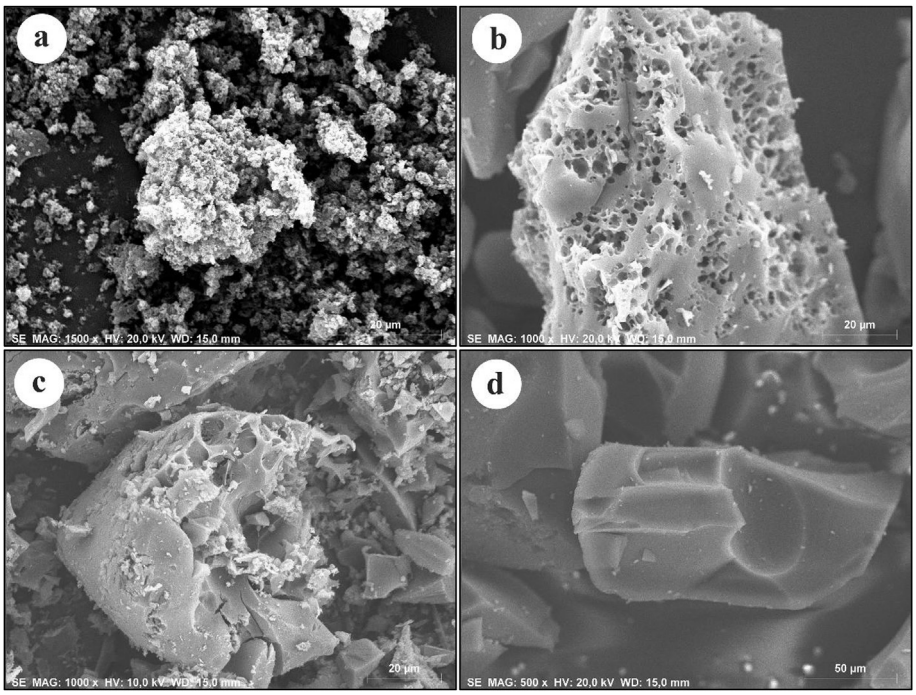

Fig. 2. SEM images of (a) PAC/Cl, (b) PAC/PTS, (c) PAC/DBS, and (d) PAC/PSS.

Table 1
Elemental analysis and atomic composition of the near surface region obtained by XPS for PAC doped with different anions.

	Elemental analysis (at.%)					Surface elemental composition (at.%)				
	C	H	N	S	O	C 1s	N 1s	O 1s	S 2p	Cl 2p
PAC/Cl	87.9	0.66	0.88	0.08	10.48	90.4	0.6	8.6	0.1	0.3
PAC/PTS	83.9	1.52	1.01	0.38	13.19	87.6	0.8	10.7	0.8	0.1
PAC/DBS	81.6	0.59	0.68	0.80	16.33	88.7	0.8	9.8	0.5	0.2
PAC/PSS	88.8	0.33	0.69	0.46	9.72	89.7	0.9	8.9	0.5	0.2
PC/Cl	–	–	–	–	–	86.4	5.5	7.8	0.1	0.2

oxygen surface groups in the carbon matrix was reported to be beneficial for the process of electrosorption mainly due to the increase of wettability [58] and the displacement of the potential of zero-charge (E_{pzc}) of the electrode [59]. The analysis of the fitted C 1s and O 1s spectra showed that surface oxygen groups of carboxylic acid (−COOH), found at 289.3 eV for C 1s and 533.7 eV for O 1, were present in all materials, however to a lower extent in PAC/DBS (Fig. 3). On the other hand, phenolic (C−OH) and/or ether (C−*O*−C) groups at 286.4 eV (C 1s) and 532.3 eV (O 1s) were most abundant in PAC/PTS and PAC/DBS, while carbonyl groups (C═O) at 287.9 eV (C 1s) and ~531 eV (O 1s) were present in all materials [30,36]. Finally, chemisorbed water was detected in all samples at about 535.5 eV (O 1s) [43]. It has been suggested that carbonyl groups are electrochemically inert and their main effect is in the shift of the $E_{pzc.}$ [60] In contrast, phenolic and carboxylic acid groups are responsible for a polar and thus hydrophilic behavior of the electrode [61]. Oxygen polar surface groups were observed in different amounts in PAC/PTS (7.3 at.%), PAC/PSS (6.1 at.%), PAC/DBS (5.6 at.%), and at lower level at PAC/Cl (4.9 at.%). These polar groups are important because they enhances hydrophilicity and wettability, which has a direct impact improving the electrode capacitance and performance for CDI since the access of water and ions to the active sites of the electrode will be facilitated, hence allowing better EDL formation [58].

The presence of nitrogen surface groups in PAC introduced by the presence of nitrogen in the PAni precursor must also be considered due to the reasons aforementioned. However, according to Table 1, the content of nitrogen after activation was relatively low (<1 at.%). As an attempt to understand why the concentration of nitrogen was drastically reduced after activation, a XPS analysis of PAni/Cl after carbonization (PC/Cl) was performed. Table 1 indicates that the amount of nitrogen was significantly higher prior activation, indicating that KOH is probably eliminating N groups from the carbon matrix at high temperatures. This result is in accordance with those obtained by Zhu et al. [44], which observed that during the pre-carbonization step at 500 °C the N groups were firstly released. Studying the activation at 700 °C and increasing the ratio of carbon and KOH from 1:2 to 1:4 (wt./wt.) these authors observed drastic reduction of the N content from 5.3 at. % to 0.9 at.%, which is a similar value found in this work. On the other hand, when the ratio of carbon and KOH was reduced to 1:1 (wt./wt.), Zhu et al. [44] observed an increase of the N content from 0.9 at.% to 5.3 at.%, indicating that KOH reacts preferentially with C atoms. Zhang et al. [43] also observed a reduction in N content when the ratio of carbonized PAni and KOH was increased from 1:2 to 1:4 during activation. It seems that the amount of KOH employed during the activation step plays an important role to control the amount of N-groups in the AC structure. On one hand, increasing the amount of KOH leads to high SSA and pore volume [43,44], while it seems to eliminate N-groups.

The fitted N1s spectra (Fig. 3) shows that the most intense component of the PAC/Cl, PAC/PTS and PAC/PSS samples, located at 400.1 eV, is related to pyrrole and pyridine sites, while PAC/DBS presents pyridinic-like nitrogen structures (C═N−C) at 398.2 eV as the strongest contribution [21]. Furthermore, the high-energy tail of the N 1s spectra indicates the presence of traces of $-N^{+}O^{-}/Cl^{-}$ structures at ~532 eV, O−N═O groups (~405 eV) and possibly also quaternary nitrogen reported to be located at 401.4 eV. The first one is related, according to Fig. 1, to a residual contribution of PAni doping sites, identified also in the Cl 2p (198.1 eV) and S 2p

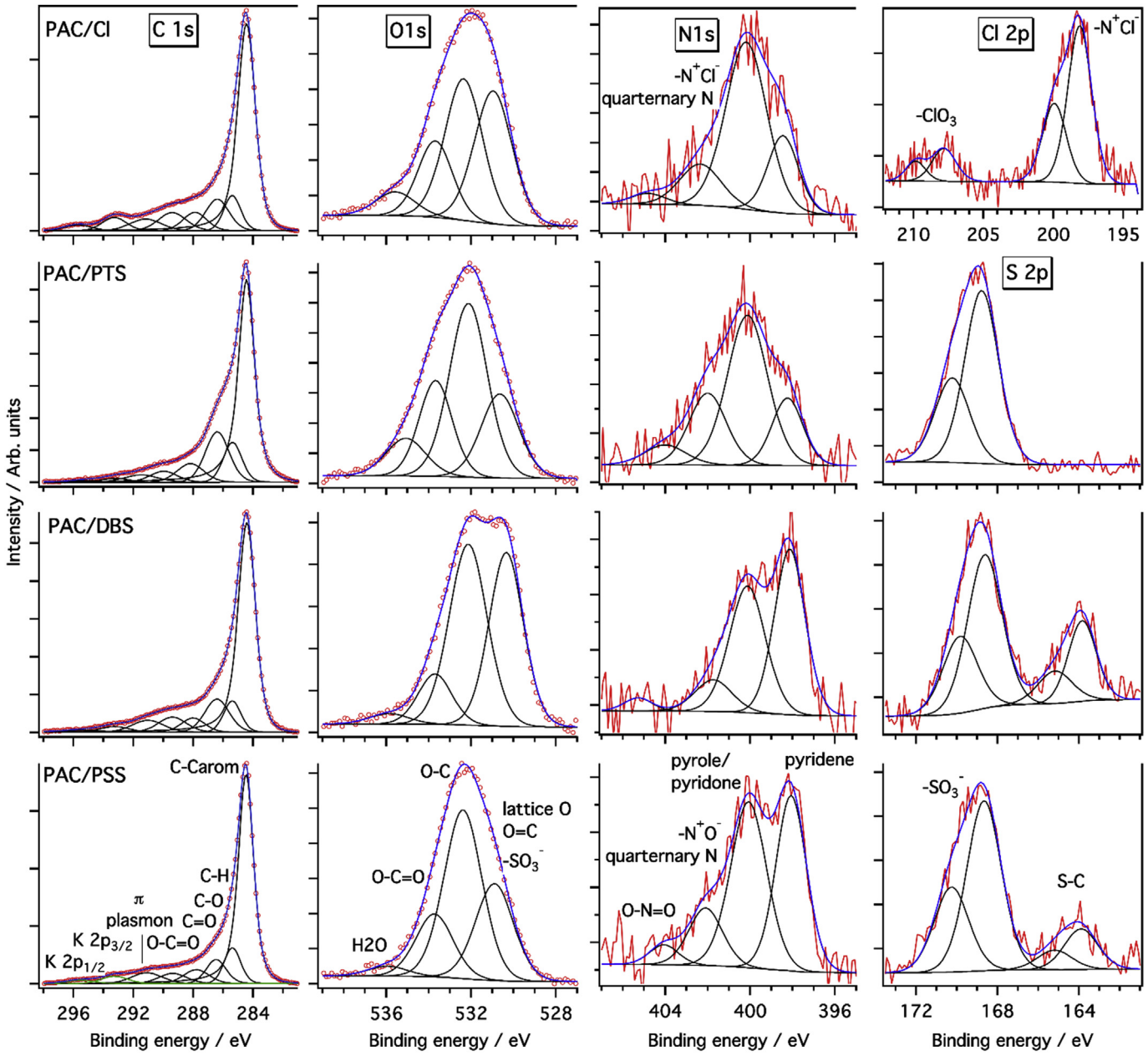

Fig. 3. Deconvoluted high resolution XPS C 1s, O 1s, N 1s, Cl 2p and S 2p spectra of PAC/Cl, PAC/PTS, PAC/DBS and PAC/PSS. (A colour version of this figure can be viewed online.)

(168.7 eV) spectra (Fig. 3), while the O–N=O groups are probably formed during the KOH activation process. Evidence for the presence of traces of potassium in the samples was found in the tail of the C 1s spectra, showing the presence of the K $2p_{3/2}$ / $2p_{1/2}$ spin-orbit pair at 293.3 eV and 295.7 eV, respectively. At this point, it is important to note that compared with other materials the PAC/PTS electrode showed the highest fraction of phenolic and/or ether groups (C 1s), pyrrole and pyridine nitrogen groups and residual $-N^{+}O^{-}$ sites (N 1s), as well as the highest proportion of chemisorbed water (O 1s), suggesting a distinct nature of this material.

Graphitic (or quaternary [21]) nitrogen is formed at high temperatures in a process that replaces carbon by nitrogen atoms in the activated carbon matrix, thus leading to an enhancement of the conductivity which could be improve the electrosorption process [21,25,62]. On the other hand, pyridine- and pyrrole-like nitrogen are located at the edge of the carbon matrix and are responsible for the pseudocapacitive effect which improves the total capacitance of the electrode and increases the SAC of the electrode [62]. Furthermore, the introduction of N could generate defects inside the carbon matrix, such as the identified residual doping sites, which would increase the SSA and improve the ability of charge-transfer inside the carbon matrix [22]. In conclusion, it seems that the main contribution of nitrogen groups for all PACs would be the introduction of pseudocapacitance due to the presence of pyridine- and pyrrole-like nitrogen.

3.2.4. Textural properties

Fig. 4(a) shows the N_2 adsorption-desorption isotherms for the different PACs. All activated carbons have a type I isotherm according to IUPAC classification [63], indicating the predominance of microporous structure. The type H4 hysteresis of PAC/Cl and PAC/DBS at higher pressures ($P/P_0 > 0.5$) indicates a considerable

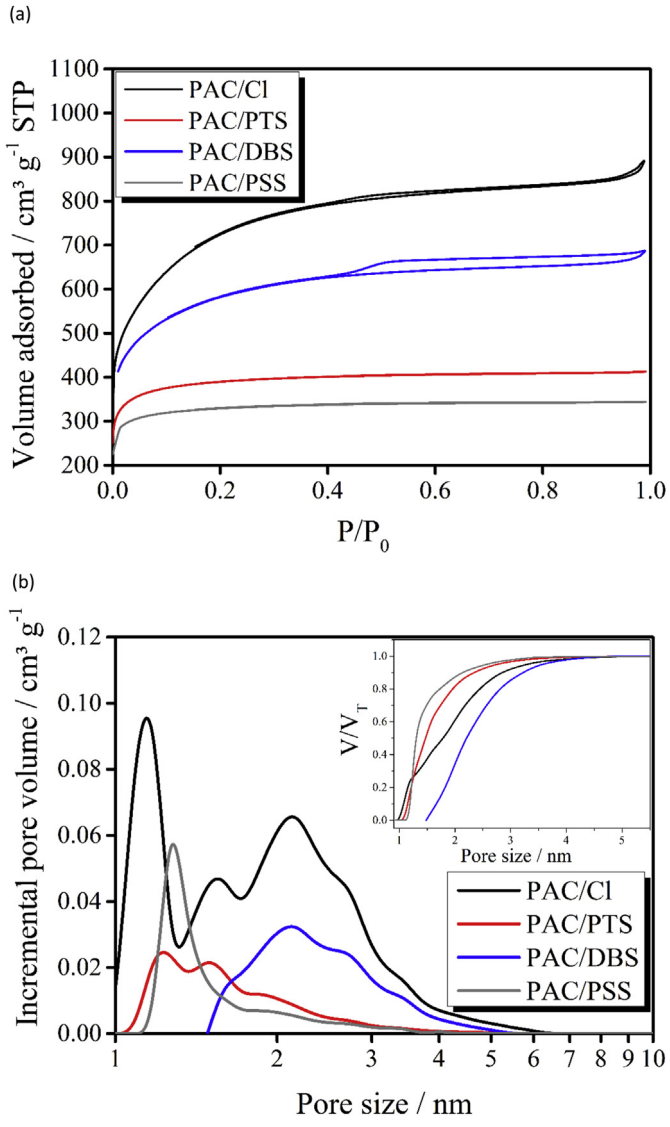

Fig. 4. (a) Isotherms of N_2 adsorption-desorption; (b) PSD. Inset: Relative cumulative pore volume distribution (V/V_T). (A colour version of this figure can be viewed online.)

contribution of mesopores.

The pore size distribution (PSD) is shown in Fig. 4(b). In accordance with the isotherms, PAC/DBS showed most part of pores with diameters larger than 2 nm, confirming the predominance of mesopores in this material. According to the IUPAC classification, micropores are related to pore diameters lower than 2 nm, mesopores as pores between 2 and 50 nm, and macropores as pores beyond 50 nm [63]. Thus, PAC/DBS was the only material that could be classified as a mesoporous material while all other PACs present their main pore contributions under 2 nm.

Table 2 Displays the textural properties determined from nitrogen adsorption-desorption isotherms shown in Fig. 4(a). As previously hypothesized, the use of different dopants for PAni preparation had a strong effect on SSA, micropore (V_{mic}) and mesopores (V_{mes}) volumes of the PACs.

The PAC/Cl presented not only the highest value of SSA (2652 $m^2\ g^{-1}$), but also the highest volume of pores (1.38 $cm^3\ g^{-1}$) and 23% of mesopores. This value of SSA was even higher than that obtained by Yan et al. [29] (1976 $m^2\ g^{-1}$) using PAni/Cl synthetized under higher acid (1.0 mol L^{-1}) and lower oxidant (0.25 mol L^{-1}) concentrations. The value of SSA obtained in this work for PAC/Cl was also very close to that obtained by Qiu et al. [65] (2923 $m^2\ g^{-1}$) for a composite of PAni/Cl and carbon nanotubes prepared under the same activation conditions. This high SSA could be ascribed to pores generated by Cl volatilization in the carbonization step at high temperature (850 °C), which was confirmed by the low content of chloride after carbonization (PC/Cl) or activation (PAC/Cl) (Table 1). The pore volume was further increased by the KOH activation, resulting in large SSA.

Large SSA was also observed for PAC/DBS, however with a considerably higher mesopore volume fraction (~60%) which could be related to micelle formation during polymerization [48], which would induce the formation of large pores after carbonization. Unlike the other anions used in this study, DBS^- is a voluminous molecule with polar and non-polar sites, which allows micelle formation according to Fig. 5. These micelles would act as a template for mesopore formation after carbonization.

Differently of PAC/Cl and PAC/DBS, PAC/PTS and PAC/PSS showed lower SSA with a higher contribution of micropores. Although PTS^- and especially PSS^- are also large molecules, they are not likely to form a micelle structure and, consequently, high mesopore formation was not expected. These results emphasize the importance of PAni dopants as template agents defining the textural characteristic of activated carbons. Although Gavrilov et al. [36] have studied carbonized PAni doped with 3,5-dinitrosalicylic and 5-sulfosalicylic acid for supercapacitors [36], their influence as a template for activated carbons have yet not been explored. Moreover, in contrast with this work, the values of SSA obtained by Gavrilov et al. [36] (300–500 $m^2\ g^{-1}$) were significantly lower, which demonstrates the importance of the activation step. Even so, Gavrilov et al. also observed the important effect of the dopants on the pore structure, SSA and nitrogen content of the carbonized PAni.

3.2.5. Electrochemical characterizations

As a first attempt to compare the different electrodes, cyclic voltammetry experiments were performed in order to analyze the capacitance and kinetics of the carbon electrodes. In this case, a more concentrated electrolyte was used in order to prevent any ion diffusion limitation and allow the comparison with other results reported in literature. Fig. 6(a) shows the CVs measured at 1.0 mV s^{-1} in NaCl 0.2 mol L^{-1}, which is the typical concentration used in CDI literature for electrochemical characterizations. At this scan rate, the CVs for PAC/Cl, PAC/PSS and CAC showed a quasi-

Table 2
Textural properties of the PAC doped with different anions, including the commercial activated carbon reference (CAC).

	SSA_{BET} ($m^2\ g^{-1}$)	V_T ($cm^3\ g^{-1}$)	V_{mic} ($cm^3\ g^{-1}$)	V_{mes} ($cm^3\ g^{-1}$)	$\%V_{mes}$
PAC/Cl	2652	1.38	1.06	0.32	23
PAC/PTS	1484	0.64	0.59	0.05	8
PAC/DBS	2041	1.05	0.44	0.61	58
PAC/PSS	1268	0.53	0.50	0.03	6
CAC	2107[a]	1.07	–	–	–

[a] Data obtained from Aslan et al. [64].

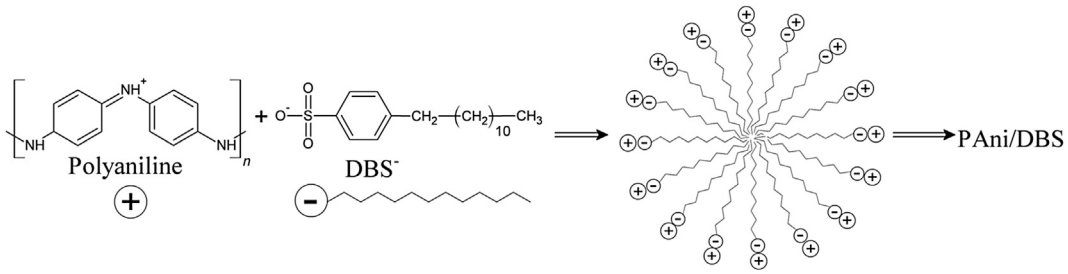

Fig. 5. Scheme of micelle formation prior to PAni/DBS polymerization.

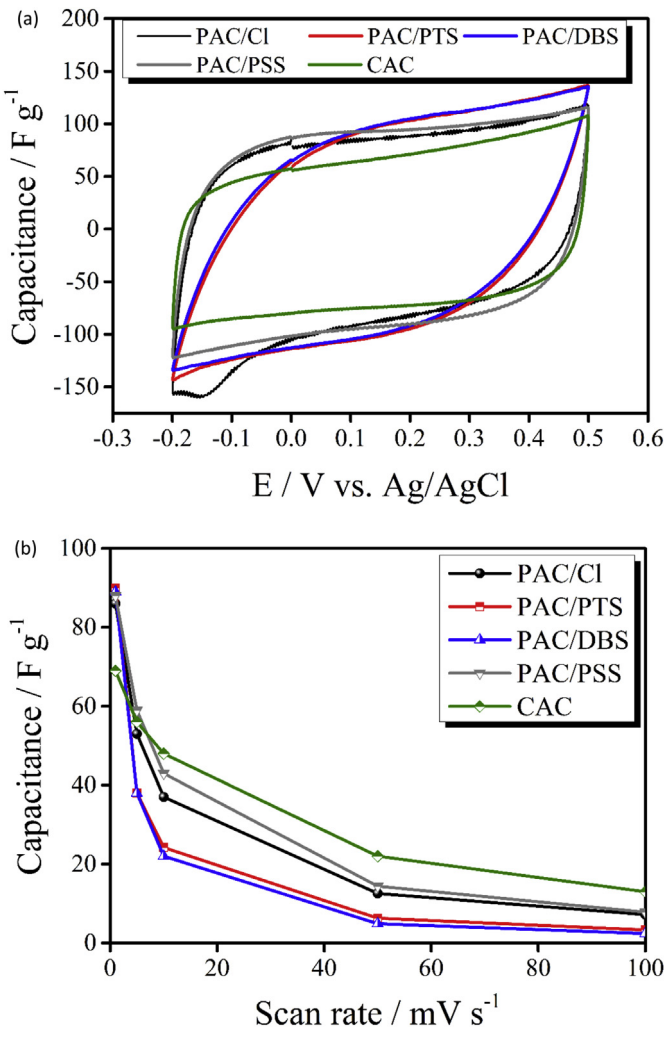

Fig. 6. (a) Cyclic voltammetries of PAC and CAC electrodes. Scan-rate: 1.0 mV s^{-1}; electrolyte: NaCl 0.2 mol L^{-1}; (b) capacitance as a function of the potential scan rate.

Table 3
Capacitance values determined from CV curves, charge-discharge and EIS measurements.

	C_{CV} / F g^{-1}	C_{CD} / F g^{-1}	C_{EIS} / F g^{-1}
PAC/Cl	87	69.3	121.5
PAC/PTS	90	121.0	122.9
PAC/DBS	89	118.6	125.0
PAC/PSS	88	108.4	113.9
CAC	69	84.5	80.0

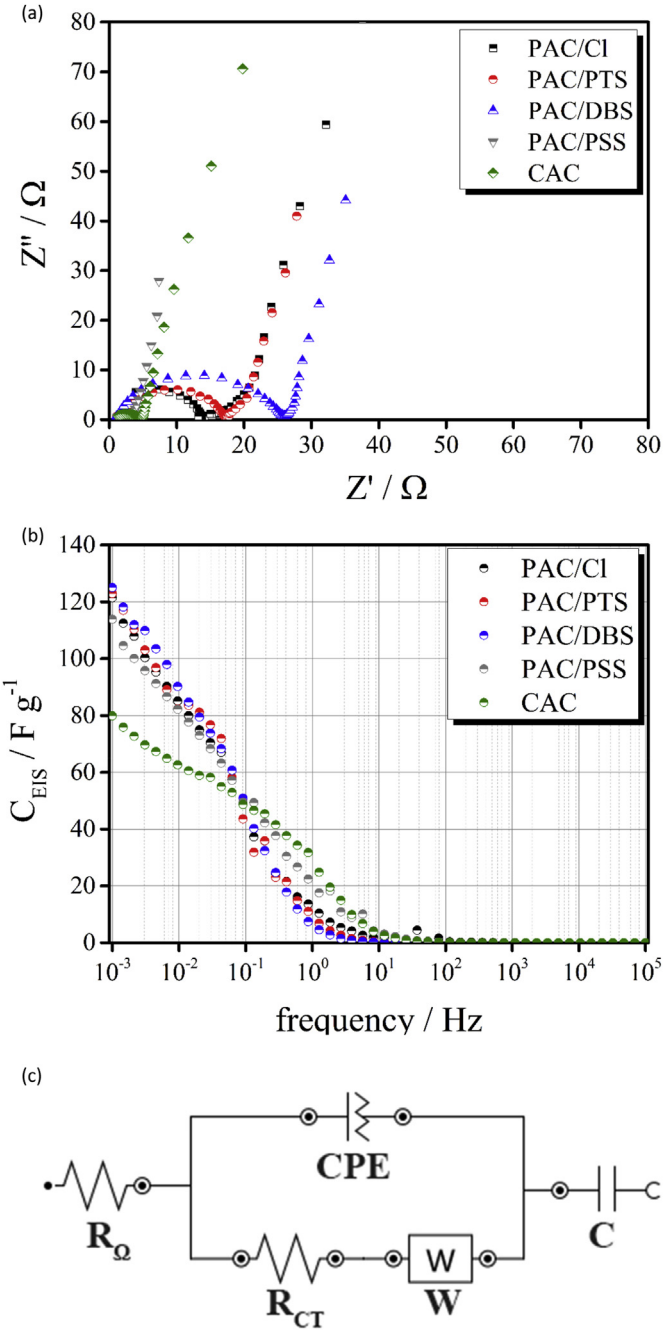

Fig. 7. Nyquist plot (a) and capacitance as a function of the frequency (b) for PAC and CAC electrodes. (c) Modified Randle equivalent circuit. Electrolyte: NaCl 0.2 mol L^{-1}; potential: 0.0 V; AC amplitude: 10 mV. (A colour version of this figure can be viewed online.)

Table 4
EIS parameters from the Nyquist plot and the modified Randle equivalent circuit.

	R_Ω / Ω	R_{CT} / Ω	A_0 / mS	Q^0 / μS s^N	N	C_C[a] / mF g^{-1}	C_d / F g^{-1}
PAC/Cl	0.71	14.7	260	1.23	0.86	0.02	162.0
PAC/PTS	0.95	16.5	790	226	0.82	2.10	174.7
PAC/DBS	0.86	25.1	1000	139	0.84	1.64	156.3
PAC/PSS	0.79	2.3	2170	320	0.75	0.58	125.7
CAC	0.80	4.0	1520	484	0.65	0.59	82.0

[a] C_C was calculated based on the values of R_{CT}, Q^0 and N.

rectangular shape, characteristic of capacitive and easily polarized materials [8,66]. This characteristic could also be observed for PAC/PTS and PAC/DBS, however with some resistivity indicated by the distortion of the CV curve [66]. Table 3 displays the specific capacitance (C_{CV}) values calculated using Equation (2). Surprisingly, all PACs exhibited similar capacitances (85–90 F g^{-1}), although the carbons presented distinguished characteristics. For instance, despite the highest SSA and percentage of mesopores of PAC/Cl and PAC/DBS, the electrode capacitances were quite similar to PAC/PTS and PAC/PSS, which are mostly composed by micropores. In this case, the surface groups probably played the most important role determining the capacitance of the electrodes. PAC/PTS and PAC/PSS had the major contribution of oxygen polar surface groups (phenol, ether and carboxylic groups), which probably enhanced the electrode wettability. In addition, PAC/PSS had major contribution of pseudocapacitive nitrogen surface groups. On the other hand, the CAC presented the lowest value of capacitance despite of its good capacitive behavior. It is also important to point out that the highest capacitance obtained in this study was very close to those obtained by other authors in literature. For instance, using similar electrolyte, Rasines et al. [6,67] obtained values of capacitance at 0.5 mV s^{-1} of 84 F g^{-1} and 97 F g^{-1} using nitrogen-doped carbon aerogel and carbon black-modified mesoporous, respectively. These values were very close to 90 F g^{-1} obtained for PAC/PTS at scan-rate of 1.0 mV s^{-1}.

CVs at different scan-rates were also carried out in order to observe the effect of mass transfer for different electrodes (Fig. 6(b)). As expected, the faster the scan rate the lower capacitance due to a diffusion limited ion transfer to the electric double layer [8]. The capacitance drop for PAC/Cl, PAC/PSS, and CAC was less pronounced when compared to the sharp drop in capacitance observed for PAC/PTS and PAC/DBS. Besides the mass transfer resistance, another possible explanation for this trend could be the higher surface conductivity of PAC/Cl, PAC/PSS, and CAC electrodes, which have a direct effect on the electric field developed in the polarized electrode. Accordingly, the higher the electrode resistivity the lower the electric field; therefore, the lower the capacitance when the scan rate is faster. Consequently, PAC/PTS and PAC/DBS, which were the most resistive electrode, showed the highest capacitance drop.

Galvanostatic charge-discharge experiments were performed applying a current density of 0.4 mA cm^{-2} (or ~0.13 A g^{-1}). The charge-discharge curves (Fig. S2) displays that PAC/PSS and CAC showed a very triangular shape which indicates good reversibility and low IR_{drop} (0.02 V for both electrodes) [21,68]. PAC/PTS and PAC/DBS showed the highest IR_{drop} (0.09 V and 0.12 V, respectively) compared with PAC/Cl (0.06 V). These results are in agreement with conclusions obtained from the CV analysis regarding to the shape of the voltammograms and confirm that PAC/PSS and CAC can be easily polarized, while PAC/DBS is the most resistive electrode. The IR_{drop} is a combination of different resistances in series including the contact between electrode and current collector, solution resistance, electrode resistivity and diffusion resistance [68]. Considering that all charge-discharge measurements were performed in the same three-electrode cell, it can be concluded that the difference in the IR_{drop} results from the major contribution of the electrode resistivity and ion diffusion resistance in the carbon matrix.

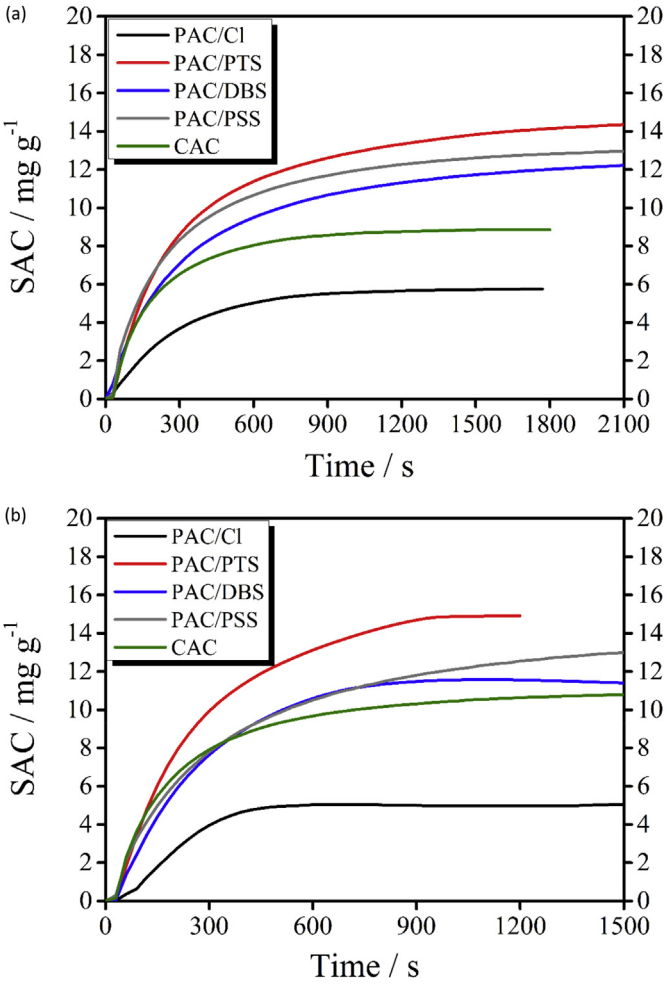

Fig. 8. SAC of PAC and CAC electrodes for desalination at 1.2 V (a) and 1.4 V (b). (A colour version of this figure can be viewed online.)

Although the capacitance determined from charge-discharge (C_{CD}) experiments were higher than the calculated from C_{CV} (except for PAC/Cl), the trend in capacitance observed for the different electrodes using the two techniques was the same. As in the CV experiments, PAC/PTS showed highest capacitance, followed by PAC/DBS and PAC/PSS. This result indicates that PAC/PTS would be the best material in terms of charge storage.

Differently of the other techniques, EIS measurements allow to evaluate both capacitance and series resistances in the electrode cell. The Nyquist plots obtained using EIS measurements for PACs and CAC are displayed in Fig. 7(a). The shape of the curves are typical of electrochemical supercapacitors [69] and present two main regions: (1) the charge-transfer region that is ascribed to the double-layer capacitance, represented by the semi-circle observed at high-frequencies and limited by the material conductivity and electrosorption kinetics and (2) mass-transfer controlled region, represented by the linear line obtained at low-frequencies [70]. Using the Nyquist plot, it is possible to measure the electric contact resistance (R_Ω) of the electrode (current collector and electrolyte resistances) and the charge-transfer resistance (R_{CT}), which is an intrinsic property of the AC electrode. The value of R_Ω and R_{CT} are

Table 5
Electrosorption parameters Q_E, η, SAC, and k_1, of the PAC and CAC electrodes.

E_{cell}	Electrode	SAC (mg g^{-1})	k_1 (x10^{-3} s^{-1})	Q_E / %	η / J mg^{-1}
1.2 V	PAC/Cl	5.8	3.3	44.5	6.9
	PAC/PTS	14.3	2.6	81.3	3.8
	PAC/DBS	12.6	2.1	74.1	7.6
	PAC/PSS	13.1	2.7	86.2	4.1
	CAC	8.9	4.4	69.7	4.2
1.4 V	PAC/Cl	5.1	5.2	32.8	12.0
	PAC/PTS	14.9	3.8	89.6	4.2
	PAC/DBS	11.7	3.9	71.5	5.1
	PAC/PSS	13.7	2.3	84.5	5.2
	CAC	10.9	4.1	73.0	4.7

obtained from the first and second intersection of the semi-circle with the abscissa, respectively [70]. The values of the resistances are displayed in Table 4. As expected, all values of $R_Ω$ were very similar because the same three-electrode cell was used for all EIS measurements. On the other hand, the values of R_{CT} were quite different and express the differences in textural and electrochemical properties of the electrode materials. For instance, the R_{CT} for PAC/DBS was 11-times higher than PAC/PSS. This trend is in agreement CV and charge-discharge results. Thus, despite the high SSA and mesoporosity of PAC/DBS, these properties were not enough to compensate the effect of its low conductivity. In contrast, PAC/PSS had the lowest SSA and mesopore ratio, and even so, presented a capacitance similar to other PACs. Similar trends were also observed by Xiong et al. [71] studying a PAni composite for supercapacitors.

Comparing the R_{CT} values in Table 4 with those reported in literature, e.g., 4.58 Ω for a N-doped copolymer [62], it can be verified that the values obtained in this work are relatively high, except for PAC/PSS (2.3 Ω).

A method widely used to describe the resistive and capacitive components of carbon electrode is the equivalent circuit fitting the Nyquist plots. The modified Randle equivalent circuit shown in Fig. 7(c) was successfully used to fit all plots of Fig. 7(a), as can be verified in Fig. S3. The values of $R_Ω$ and R_{CT} were identical with those already presented in Table 4. The *CPE* element was used because in double layer capacitors a perfect semicircle ascribed to an ideal capacitor is seldom observed. The non-ideality of the double layer capacitor is typical of electrochemical charging processes and may be related to the non-uniformity of electrode thickness, variation of the microscopic charge-transfer rate, adsorption processes, or surface roughness [72]. The values of Q^0 and N were obtained from the *CPE* impedance described by Equation (8), which is a modification of Equation (4):

$$Z'' = \frac{1}{(j\omega)^N Q^0} \tag{8}$$

In this Equation, j is the imaginary number, N is a constant in the range of $0 \leq N \leq 1$ and Q^0 (S s^N) has the numerical value of admittance at $\omega = 1$ rad s^{-1}. When $N = 1$, $Q^0 = C_{EIS}$ and Equation (9) becomes exactly the same Equation (4). However, as can be observed in Table 4, N was always lower than unit, reaching the lowest value for CAC. In order to obtain the capacitance associated to the *CPE* (C_C), Equation (9) [73] was used in which m_{WE} is the mass of the working electrode.

$$C_C = \frac{(Q^0)^{\frac{1}{N}} (R_{CT})^{\frac{(1-N)}{N}}}{m_{WE}} \tag{9}$$

The C_C is the capacitance at the interface electrolyte/electrode at high frequencies [74,75], while the capacitance of the capacitor

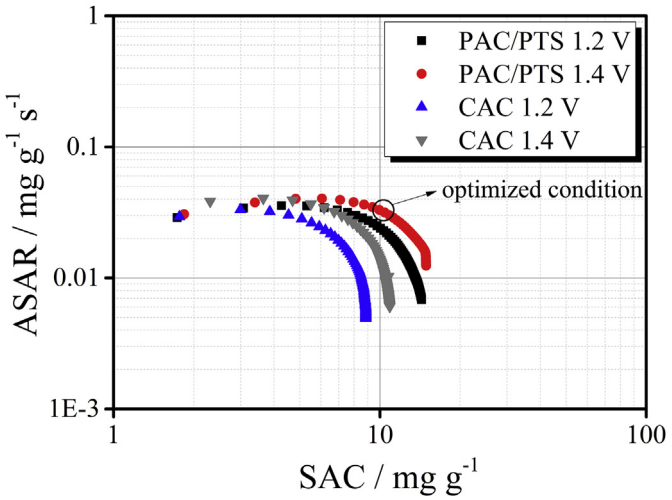

Fig. 9. ASAR *vs.* SAC for PAC/PTS and CAC at 1.2 and 1.4 V. (A colour version of this figure can be viewed online.)

element (C_d) in the equivalent circuit is associated to the capacitance developed inside the micropores of the carbon electrode [74,76]. According to Table 4, it can be observed that PAC/PTS has the highest values of C_C and C_d among the electrodes studied; which C_d represents the main contribution to the total electrode capacitance.

Another component used to describe the EIS spectra is the Warburg element (W), which is a diffusion element used to describe the effect of ion migration in the interior of pores of the carbon film [74,77]. The Warburg element was associated in series with the R_{CT} because the Warburg region is located between the semicircle and the spike in the Nyquist plot [78]. The element A_0 displayed in Table 4 was obtained from the circuit fitting for the Warburg element and represent the admittance, which is the inverse of the Warburg impedance. The higher A_0 the higher the conductivity for the ion diffusion inside the pores. According to Table 4, while PAC/PSS showed the highest admittance (or the lowest Warburg resistance), PAC/Cl showed the lowest values.

Fig. 7(b) shows the capacitance obtained using EIS measurements as function of frequency. At high frequencies, there was a predominance of the ohmic resistance, and the capacitances of the electrode materials were very low. This is expected since the ions do not have enough time to reach the pores and be stored in the EDL. As the frequency decreases they are able to reach the micropores, thus increasing significantly the capacitance, which reaches a maximum value at the lowest frequency [79].

3.2.6. Electrosorption experiments

Desalination experiments were performed in a batch operational mode at different cell voltages (E_{cell}). The electrode performance at 1.2 V and 1.4 V (Fig. 8(a) and (b), respectively) is displayed in terms of specific adsorption capacity (SAC) against time for PAC and CAC electrodes. It can be observed that an increase of the applied voltage from 1.2 V to 1.4 V led to an increase of the SAC for PAC/PTS, PAC/PSS, and CAC electrodes. This enhancement can be ascribed to an EDL thickness reduction at higher voltages, which prevents the EDL to overlap, and consequently, increases the ions storage in the micropores [80]. In contrast, for PAC/Cl and PAC/DBS electrodes, SAC decreased applying 1.4 V, what could suggest the occurrence of Faradaic reactions that interfere in the conductivity measurement due to the release of new ionic species (Fig. 8(b)) [5]. The generation of

protons due to water electrolysis or carbon electrode oxidation has been often reported in the CDI literature [81–86]. In addition, the occurrence of certain species such as H_2O_2 or ClO_3^- has been also identified in electrosorption experiments. In these studies, the likelihood of inducing Faradaic reactions has been demonstrated to rise with the increase of the applied cell potential. Moreover, higher concentrations of these species were found when higher cell voltages were applied, producing, as a consequence, a more disruptive effect on the conductivity measurements [87].

The different response of these electrodes to the application of relatively high voltages (1.4 V) could be attributed to two main causes: (i) The cell setup could introduce a series of resistances between the pair of electrodes such as the electric contact current between collector/substrate, flowing channel, and electrolyte resistivity. These resistances could be responsible for a potential drop throughout the cell and this would reduce the electrode potential preventing in this fashion the occurrence of faradaic reactions [25,88]. (ii) Another hypothesis is based on the electrode electrochemical stability and the shifting of the electrode potential due to the presence of certain surface groups that might avoid or promote the occurrence of faradaic reactions [5]. In this sense, Cohen et al. [84] and Lado et al. [87] showed how the presence of surface oxygen groups shifted the anode potential of the carbon electrodes inducing the oxidation of the carbon electrode, proton generation and pH drop.

In the present study, all the experiments were performed using the same CDI cell configuration and, consequently, cell resistances were always the same. Therefore, considering that PAC/PTS, PAC/PSS and CAC showed higher electrochemical stability at higher cell voltages, the authors attribute the differences in SAC to the potential shifting that induced the occurrence of faradaic reactions.

Comparing the values of capacitance shown in Table 3 with SAC values from Table 5, it can be observed that only the charge-discharge technique was able to predict the electrosorption trend in terms of SAC, i.e., $C_{CD,\ PTS} > C_{CD,\ PSS} > C_{CD,\ DBS} > C_{CD,\ CAC} > C_{CD,\ Cl}$ and, consequently, $SAC_{PTS} > SAC_{PSS} > SAC_{DBS} > SAC_{CAC} > SAC_{Cl}$. These results suggest that this technique would be rather used to predict the performance of the carbon electrodes for CDI. Although CV capacitance (and C_{EIS} as well) has been frequently used to predict the electrode performance in CDI, in this case this technique failed. Surprisingly, PAC/Cl had the worst electrosorption performance despite its high surface area (Table 2), which can be explained by the lower content of polar oxygen groups (Table 1). As discussed in section 2.2.3, polar oxygen groups play a paramount influence on the electrode wettability and, consequently, on the electrode performance.

The kinetic constant of pseudo first order (k_1) of the process carried out using the different electrodes was evaluated by the fitting of the electrosorption curves (Fig. 8). PAC/Cl was by far the electrode that showed the lowest SAC but with fast electrosorption kinetics, which can probably be ascribed to its high conductivity (Table 4), and large exposed area (Fig. 2(a)). This same trend was also observed for CAC, which presented the highest conductivity among all ACs and displayed the highest k_1 at 1.2 V. On the other hand, the lowest value of SAC observed for PAC/Cl can be attributed to the deficiency of polar surface groups (phenol, ether and carboxylic), which increases hydrophobicity (low wettability) and thus prevent the access of ions to the micropores. Furthermore, its lowest pyrrole- and pyridinic-like nitrogen content (Table 1 and Fig. 3) prevents pseudocapacitive processes, which would contribute to the lowest value of SAC of PAC/Cl. All other PAC electrodes showed similar values of SAC ranging from 12 to 15 mg g^{-1}. It is interesting to note that despite the high SSA and mesopore ratio of PAC/DBS, the highest content of polar and pseudocapacitive surface groups of PAC/PTS and PAC/PSS, respectively, seems to provide easy access to the electrosorption sites, which resulted in the best performance of these electrodes in terms of SAC [58]. In the case of PAC/PTS, a clear evidence of its hydrophilicity is the high proportion of chemisorbed water demonstrated by its O 1s XPS spectra. Therefore, the synergetic effect of different material characteristics such as active surface groups, electric properties and texture might be responsible for determining the electrode performance.

The electrosorption kinetics is another important characteristic that influences the operation of a CDI cell. As the desalination process presupposes several electrosorption and regeneration cycles, the water recovery is directly affected by the time required for sorption and desorption. CDI Ragone Plot is widely applied as important tool to evaluate simultaneously the kinetics and electrosorption capacity by using the average salt adsorption rate (ASAR) and SAC, respectively. According to Fig. 9, PAC/PTS presents the highest values of SAC compared to CAC. The points displayed in Fig. 9 represent a complete electrosorption cycle indicating how SAC and ASAR varied with time. The curves displaced in the upper-right corner of the Ragone plot indicates the better electrode performance [89]. Although both electrodes display slightly similar electrosorption kinetics, PAC/PTS outperforms CAC in terms of capacity, especially at 1.4 V. The optimized condition using PAC/PTS was achieved for SAC 9.9 mg g^{-1} and ASAR 0.033 mg g^{-1} s^{-1} at 1.4 V, after 5 min of the beginning of the electrosorption process.

Besides SAC and the Ragone plot, the desalination process was also evaluated regarding to charge efficiency (Q_E) and specific energy consumption (η), which are parameters that indicate whether the charge supplied to the CDI system has being effectively used for the electrosorption process and how much energy is required per mass of salt removed (Equation (7)), respectively. In order to properly evaluate Q_E, only the current effectively used for electrosorption was used in Equation (6), i.e., the leakage current, which is a parasitic process commonly associated to redox reactions, was subtracted from the total current [23,58,90]. In the case of η, the leakage current was considered since it contributes to the overall energy consumption.

Table 5 shows the values of Q_E and η obtained for the NaCl electrosorption at different cell voltages using the PAC and CAC electrodes. In all cases, the values of Q_E were lower than the 100% valid for an ideal system in which the entire charge supplied by the external source is used for ion separation of monovalent salts such as NaCl. However, due to energy losses, faradaic reactions [91], and the presence of co-ions [92], this value hardly reaches more than 90%.

Interestingly, PAC/PTS showed an increase in Q_E when E_{cell} was increased from 1.2 V to 1.4 V, confirming a minor contribution of faradaic reactions to the total current of this electrode. PAC/PSS and PAC/DBS had only a small drop in Q_E (2–3%), in contrast with the PAC/Cl that showed a strong decrease (12%). The charge efficiency drop observed for PAC/Cl is in accordance with the decrease of the SAC values when the applied voltage was raised from 1.2 to 1.4 V and it supports the hypothesis that faradaic reactions is the main process explaining the SAC reduction. In addition, the CDI process carried out using PAC/Cl at 1.4 V demanded almost twice more energy than at 1.2 V, which can be attributed not only to faradaic reactions but also to resistive dissipation (heat loss) [93].

Surprisingly, PAC/DBS showed a simultaneous decrease of Q_E and η when the cell voltage was increased. One could think that a charge efficiency drop would lead to the increase of the energy consumption, however, higher values of leakage current were measured at 1.2 V (11.2 mA) than at 1.4 V (6.4 mA), which explains the reduction of the energy consumption when the cell voltage was

Table 6
SAC obtained using different carbon materials in a CDI process.

Authors	Electrode material	Salt concentration / mg L^{-1}	Cell voltage	SAC (mg g^{-1})
Gu et al., 2014 [21]	N-doped graphene	500	2.0	21.9
Liu et al., 2015 [22]	N-doped nanofiber graphene	500	1.2	11.6
Liu et al., 2015 [95]	N-doped carbon nanospheres	500	1.2	13.7
Porada et al., 2015 [23]	N-doped biomass	300	1.2	15.0
Xu et al., 2015 [25]	N-doped graphene	500	1.2	12.8
Xu et al., 2015 [96]	N-doped graphene sponge	500	1.2	21.0
Xu et al., 2015 [97]	Graphene sponge	500	1.2	14.6
Kumar et al., 2016 [9]	Carbon aerogel	500	1.2	10.5
Zhao et al., 2016 [68]	Hollow carbon nanospheres	500	1.4	13.0
Li et al., 2016 [24]	N-doped carbon sponge	500	1.2	16.1
Li et al., 2016 [62]	N-doped copolymer	500	1.2	13.8
Shi et al., 2016 [98]	Three-dimensional graphene	500	1.2	12.4
		500	1.6	17.1
This work	PAC/PTS	600	1.2	14.3
		600	1.4	14.9

increased. On contrary, for CAC electrode, Q_E and η increased with the cell voltage, indicating that despite of the efficient use of the supplied charge to remove ions, the increase of the leakage current at 1.4 V (from 3.2 mA at 1.2 V to 3.9 mA at 1.4 V) lead to an increase of η. Concerning PAC/PTS, only a slight increase of η was observed at 1.4 V, suggesting an improved stability of this electrode material.

Another way to analyze the effect of the cell voltage on the electrode performance was proposed by Kim et al. [94] (Equation (10)). Using this method, the capacitance can be obtained from charge-discharge experiments to estimate the highest value of SAC (D_c). The ratio between the values of SAC, determined from the electrosorption experiments, and D_c is referred as capacitance efficiency (ε).

$$D_c = 1000\frac{C_{CD}\ Ecell\ M_w}{4F} \tag{10}$$

In Equation (10), D_c is in mg g^{-1} and M_w is the molecular weight of NaCl (58.5 g mol^{-1}). As can be observed in Table S3, the capacitance overestimate the SAC values in all cases, what was expected since the experiments of charge-discharge were carried out in a more concentrated solution (0.2 mol L^{-1} NaCl). Moreover, capacitance measurements consider that all current have been effectively used for electrosorption, excluding the leakage current. The same reason supports the increase of D_c values when the applied voltage was boosted due to since the negative effect of the faradaic reactions on charge efficiency and SAC values were not considered by this parameter. This argument was clearly appreciated in the case of PAC/Cl electrodes, where the increase of the cell voltage led to contradictory trends. Thus, while D_c values accompanied the applied potential increment, the drop in SAC values are supported by the previous results that suggested the occurrence of faradaic reactions as the cause of the salt electrosorption decay. These factors led to the lowest ε value displayed by PAC/Cl (45.9% at 1.2 V and 34.6% at 1.4 V). The same trend was observed for PAC/DBS which exhibited low ε at 1.4 V (46.4%), indicating the occurrence of faradaic reactions at this cell voltage. On the other hand, PAC/PSS and PAC/PTS showed a good correlation between D_c and SAC (58–67%). Regarding PAC/PSS, the values of SAC seems to be boosted by its high conductivity (low R_{CT}) and pseudocapacitive surface groups, therefore this material achieved almost 70% of the value of predicted by the capacitance (D_c).

Interestingly, except for CAC, in all cases the application of 1.4 V resulted in lower ε, even for PAC/PTS. Despite the higher values of SAC observed using PAC/PTS at 1.4 V, this enhancement was not proportional to the difference estimated by D_c. This suggests that despite of SAC enhancement after increasing the voltage from 1.2 V to 1.4 V, the values of SAC were still underestimated, probably due to a minor contribution of faradaic reactions. As a final remark, CAC, unlike the other electrodes, experienced a capacitance efficiency improvement at 1.4 V, suggesting that CAC presents higher electrochemical stability at high cell voltages than the PAC electrodes. The results suggest that capacitance efficiency analysis seems to be a useful tool for estimating the faradaic reactions effect on the CDI performance at different cell voltages.

In summary, PAC/PTS gathered most of the best results required for CDI: high salt electrosorption capacity (14–15 mg g^{-1}), high charge efficiency (81–90%), and low energy consumption (3.8–4.2 J mg^{-1}). Finally, Table 6 compares PAC/PTS with values of SAC obtained by other authors employing different electrode materials (most of them, N-doped carbon) under similar operational conditions. The comparison reveals that PAC/PTS is among the best electrodes regarding the electrosorption capacity, although the SAC reported for N-doped graphene electrodes surpasses the PAC/PTS; however, PAni can be easily prepared and the low-cost of the monomer with respect to the graphene materials makes PAC/PTS a promising material for CDI applications.

4. Conclusions

In this study, new activated carbon materials have been prepared using PAni doped with different anions as precursor. By the best of our knowledge, this was the first time that different dopant anions were used as template to prepare high-performance electrodes for CDI. Structural analysis of the PAC characteristics such as morphology, SSA, conductivity and surface groups were highly dependent on the anion used for PAni doping.

Although one of the initial ideas of using PAni as precursor was to obtain an activated carbon with high nitrogen content, the activation using KOH at high temperature removed most part of it. On the other hand, the high oxygen content in the PACs, mainly in PAC/PTS, seemed to play the most important role improving the PAC wettability by the introduction of surface polar groups such as phenolic and carboxylic groups.

Regarding to electrosorption process, PAC/PTS, PAC/PSS, and PAC/DBS showed similar removal efficiencies, while PAC/Cl presented by far the lowest value of SAC. Although PAC/PTS presented low specific surface area and mesopore ratio among the electrodes, the values of SAC (14.3 mg g^{-1} at 1.2 V and 14.9 mg g^{-1} at 1.4 V), Q_E (81.9% and 89.6% at 1.2 V and 1.4 V, respectively), and η (3.8 J mg^{-1} at 1.2 V) outperformed those for all the other electrodes due to its high polar surface group content. Considering simplicity and low-cost preparation of PAC/PTS, it can be considered as very promising candidate for large-scale CDI applications.

Acknowledgments

The authors are grateful to São Paulo Research Foundation (FAPESP) – Grant 2015/16107-4), Coordination for the Improvement of Higher Education Personnel (CAPES) and National Council of Technological and Scientific Development (CNPq) for the financial support. Moreover, R. L. Zornitta acknowledges FAPESP (Grant 2015/26593-3), CNPq and Carolina Foundation by the PhD fellowship. J.J. Lado acknowledges CAPES for the Science without Borders fellowship. The authors also thank Jéssica A. Oliveira and EMBRAPA Instrumentação for the FTIR analysis.

Appendix A. Supplementary data

Supplementary data related to this article can be found at http://dx.doi.org/10.1016/j.carbon.2017.07.071.

References

[1] M.A. Anderson, A.L. Cudero, J. Palma, Capacitive deionization as an electrochemical means of saving energy and delivering clean water. Comparison to present desalination practices: will it compete? Electrochim. Acta 55 (2010) 3845–3856, http://dx.doi.org/10.1016/j.electacta.2010.02.012.
[2] F.A. AlMarzooqi, A.A. Al Ghaferi, I. Saadat, N. Hilal, Application of Capacitive Deionisation in water desalination: a review, Desalination 342 (2014) 3–15, http://dx.doi.org/10.1016/j.desal.2014.02.031.
[3] D.V. Fix, Capacitive Deionization of NH_4ClO_4 Solutions with Carbon Aerogel Electrodes, vol. 26, 1996, pp. 1007–1018.
[4] C. Tsouris, R. Mayes, J. Kiggans, K. Sharma, S. Yiacoumi, D. DePaoli, Mesoporous carbon for capacitive deionization of saline water, Env. Sci. Technol. 45 (2011) 10243–10249, http://dx.doi.org/10.1021/es201551e.
[5] R.L. Zornitta, J.J. Lado, M.A. Anderson, L.A.M. Ruotolo, Effect of electrode properties and operational parameters on capacitive deionization using low-cost commercial carbons, Sep. Purif. Technol. 158 (2016) 39–52, http://dx.doi.org/10.1016/j.seppur.2015.11.043.
[6] G. Rasines, P. Lavela, C. Macías, M.C. Zafra, J.L. Tirado, C.O. Ania, Mesoporous carbon black-aerogel composites with optimized properties for the electro-assisted removal of sodium chloride from brackish water, J. Electroanal. Chem. 741 (2015) 42–50, http://dx.doi.org/10.1016/j.jelechem.2015.01.016.
[7] Y. Oren, Capacitive deionization (CDI) for desalination and water treatment — past, present and future (a review), Desalination 228 (2008) 10–29, http://dx.doi.org/10.1016/j.desal.2007.08.005.
[8] G. Rasines, P. Lavela, C. Macías, M. Haro, C.O. Ania, J.L. Tirado, Electrochemical response of carbon aerogel electrodes in saline water, J. Electroanal. Chem. 671 (2012) 92–98, http://dx.doi.org/10.1016/j.jelechem.2012.02.025.
[9] R. Kumar, S.S. Gupta, S. Katiyar, V.K. Raman, S.K. Varigala, T. Pradeep, A. Sharma, Carbon aerogels through organo-inorganic co-assembly and their application in water desalination by capacitive deionization, Carbon N. Y. 99 (2016) 375–383, http://dx.doi.org/10.1016/j.carbon.2015.12.004.
[10] C.-L. Yeh, H.-C. Hsi, K.-C. Li, C.-H. Hou, Improved performance in capacitive deionization of activated carbon electrodes with a tunable mesopore and micropore ratio, Desalination 367 (2015) 60–68, http://dx.doi.org/10.1016/j.desal.2015.03.035.
[11] S. Porada, L. Weinstein, R. Dash, A. van der Wal, M. Bryjak, Y. Gogotsi, et al., Water desalination using capacitive deionization with microporous carbon electrodes, ACS Appl. Mater. Interfaces 4 (2012) 1194–1199, http://dx.doi.org/10.1021/am201683j.
[12] J.-H. Lee, H.-J. Ahn, D. Cho, J.-I. Youn, Y.-J. Kim, H.-J. Oh, Effect of surface modification of carbon felts on capacitive deionization for desalination, Carbon Lett. 16 (2015) 93–100, http://dx.doi.org/10.5714/CL.2015.16.2.093.
[13] Z.H. Huang, M. Wang, L. Wang, F. Kang, Relation between the charge efficiency of activated carbon fiber and its desalination performance, Langmuir 28 (2012) 5079–5084, http://dx.doi.org/10.1021/la204690s.
[14] X.Z. Wang, M.G. Li, Y.W. Chen, R.M. Cheng, S.M. Huang, L.K. Pan, et al., Electrosorption of NaCl solutions with carbon nanotubes and nanofibers composite film electrodes, Electrochem. Solid-State Lett. 9 (2006) E23, http://dx.doi.org/10.1149/1.2213354.
[15] L. Yang, Z. Shi, W. Yang, Enhanced capacitive deionization of lead ions using air-plasma treated carbon nanotube electrode, Surf. Coatings Technol. 251 (2014) 122–127, http://dx.doi.org/10.1016/j.surfcoat.2014.04.012.
[16] J.J. Lado, J.J. Wouters, M.I. Tejedor-Tejedor, M.A. Anderson, E. Garcia-Calvo, Asymmetric capacitive deionization utilizing low surface area carbon electrodes coated with nanoporous thin-films of Al2O3 and SiO2, J. Electrochem. Soc. 160 (2013) E71–E78, http://dx.doi.org/10.1149/2.094308jes.
[17] K. Laxman, M.T.Z. Myint, H. Bourdoucen, J. Dutta, Enhancement in ion adsorption rate and desalination efficiency in a capacitive deionization cell through improved electric field distribution using zinc oxide nanorods coated activated carbon cloth electrodes, ACS Appl. Mater. Interfaces (2014) 6–13, http://dx.doi.org/10.1021/am501041t.
[18] Y.-J. Kim, J.-H. Choi, Improvement of desalination efficiency in capacitive deionization using a carbon electrode coated with an ion-exchange polymer, Water Res. 44 (2010) 990–996, http://dx.doi.org/10.1016/j.watres.2009.10.017.
[19] C. Yan, L. Zou, R. Short, Polyaniline-modified activated carbon electrodes for capacitive deionisation, Desalination 333 (2014) 101–106, http://dx.doi.org/10.1016/j.desal.2013.11.032.
[20] L. Weinstein, R. Dash, Capacitive Deionization: Challenges and Opportunities, 2013, pp. 34–37.
[21] X. Gu, Y. Yang, Y. Hu, M. Hu, J. Huang, C. Wang, Nitrogen-doped graphene composites as efficient electrodes with enhanced capacitive deionization performance, RSC Adv. 4 (2014) 63189–63199, http://dx.doi.org/10.1039/C4RA11468J.
[22] Y. Liu, X.T. Xu, T. Lu, Z. Sun, D.H.C. Chua, L.K. Pan, Nitrogen-doped electrospun reduced graphene oxide-carbon nanofiber composite for capacitive deionization, RSC Adv. 5 (2015) 34117–34124, http://dx.doi.org/10.1039/C5RA00620A.
[23] S. Porada, F. Schipper, M. Aslan, M. Antonietti, V. Presser, T.P. Fellinger, Capacitive deionization using biomass-based microporous salt-templated heteroatom-doped carbons, ChemSusChem. 8 (2015) 1823, http://dx.doi.org/10.1002/cssc.201500696.
[24] G.X. Li, P.X. Hou, S.Y. Zhao, C. Liu, H.M. Cheng, A flexible cotton-derived carbon sponge for high-performance capacitive deionization, Carbon N. Y. 101 (2016) 1–8, http://dx.doi.org/10.1016/j.carbon.2015.12.095.
[25] X. Xu, L. Pan, Y. Liu, T. Lu, Z. Sun, Enhanced capacitive deionization performance of graphene by nitrogen doping, J. Colloid Interface Sci. 445 (2015) 143–150, http://dx.doi.org/10.1016/j.jcis.2015.01.003.
[26] P. Chen, T.Y. Xiao, Y.H. Qian, S.S. Li, S.H. Yu, A nitrogen-doped graphene/carbon nanotube nanocomposite with synergistically enhanced electrochemical activity, Adv. Mater 25 (2013) 3192–3196, http://dx.doi.org/10.1002/adma.201300515.
[27] X. Yang, D. Wu, X. Chen, R. Fu, Nitrogen-enriched nanocarbons with a 3-D continuous mesopore structure from polyacrylonitrile for supercapacitor application, J. Phys. Chem. C 114 (2010) 8581–8586, http://dx.doi.org/10.1021/jp101255d.
[28] M. Trchová, E.N. Konyushenko, J. Stejskal, J. Kovářová, G. Ćirić-Marjanović, The conversion of polyaniline nanotubes to nitrogen-containing carbon nanotubes and their comparison with multi-walled carbon nanotubes, Polym. Degrad. Stab. 94 (2009) 929–938, http://dx.doi.org/10.1016/j.polymdegradstab.2009.03.001.
[29] J. Yan, T. Wei, W. Qiao, Z. Fan, L. Zhang, T. Li, et al., A high-performance carbon derived from polyaniline for supercapacitors, Electrochem. Commun. 12 (2010) 1279–1282, http://dx.doi.org/10.1016/j.elecom.2010.06.037.
[30] L. Li, E. Liu, J. Li, Y. Yang, H. Shen, Z. Huang, et al., A doped activated carbon prepared from polyaniline for high performance supercapacitors, J. Power Sources 195 (2010) 1516–1521, http://dx.doi.org/10.1016/j.jpowsour.2009.09.016.
[31] A.B. Fuertes, T.A. Centeno, Mesoporous carbons with graphitic structures fabricated by using porous silica materials as templates and iron-impregnated polypyrrole as precursor, J. Mater. Chem. 15 (2005) 1079–1083, http://dx.doi.org/10.1039/b416007j.
[32] E. Frackowiak, V. Khomenko, K. Jurewicz, K. Lota, F. Béguin, Supercapacitors based on conducting polymers/nanotubes composites, J. Power Sources 153 (2006) 413–418, http://dx.doi.org/10.1016/j.jpowsour.2005.05.030.
[33] R.L. Zornitta, G. Pincelli, L.A.M. Ruotolo, Modificação do polímeros comdutor polianilina para uso como trocador catiônico, Quim. Nov. 37 (2014) 1459–1464.
[34] C. Yan, L. Zou, R. Short, Single-walled carbon nanotubes and polyaniline composites for capacitive deionization, Desalination 290 (2012) 125–129, http://dx.doi.org/10.1016/j.desal.2012.01.017.
[35] Gang Wu, Karren L. More, Christina M. Johnston, P. Zelenay, High-performance electrocatalysts for oxygen reduction derived from polyaniline, Iron, Cobalt, Sci. 80 (322) (2011) 443–448, http://dx.doi.org/10.1126/science.1200832.
[36] N. Gavrilov, I.A. Pasti, M. Vujkovic, J. Travas-Sejdic, G. Ciric-Marjanovic, S.V. Mentus, High-performance charge storage by N-containing nanostructured carbon derived from polyaniline, Carbon N. Y. 50 (2012) 3915–3927, http://dx.doi.org/10.1016/j.carbon.2012.04.045.
[37] Y. Jia, J. Jiang, K. Sun, Pyrolysis of polyaniline-poly(styrene sulfonate) hydrogels to prepare activated carbons for the adsorption of vitamin B12, J. Anal. Appl. Pyrolysis 111 (2015) 247–253, http://dx.doi.org/10.1016/j.jaap.2014.10.023.
[38] M. Yang, B. Cheng, H. Song, X. Chen, Preparation and electrochemical performance of polyaniline-based carbon nanotubes as electrode material for supercapacitor, Electrochim. Acta 55 (2010) 7021–7027, http://dx.doi.org/10.1016/j.electacta.2010.06.077.
[39] X. Xiang, E. Liu, Z. Huang, H. Shen, Y. Tian, C. Xiao, et al., Preparation of activated carbon from polyaniline by zinc chloride activation as supercapacitor electrodes, J. Solid State Electrochem 15 (2011) 2667–2674, http://dx.doi.org/10.1007/s10008-010-1258-7.
[40] K.S. Kim, S.J. Park, Easy synthesis of polyaniline-based mesoporous carbons and their high electrochemical performance, Microporous Mesoporous Mater 163 (2012) 140–146, http://dx.doi.org/10.1016/j.micromeso.2012.04.047.
[41] M. Vujković, N. Gavrilov, I. Pašti, J. Krstić, J. Travas-Sejdic, G. Ćirić-Marjanović, et al., Superior capacitive and electrocatalytic properties of carbonized

nanostructured polyaniline upon a low-temperature hydrothermal treatment, Carbon N. Y. 64 (2013) 472–486, http://dx.doi.org/10.1016/j.carbon.2013.07.100.
[42] C. Long, D. Qi, T. Wei, J. Yan, L. Jiang, Z. Fan, Nitrogen-doped carbon networks for high energy density supercapacitors derived from polyaniline coated bacterial cellulose, Adv. Funct. Mater 24 (2014) 3953–3961, http://dx.doi.org/10.1002/adfm.201304269.
[43] Z. Zhang, Z. Zhou, H. Peng, Y. Qin, G. Li, Nitrogen- and oxygen-containing hierarchical porous carbon frameworks for high-performance supercapacitors, Electrochim. Acta 134 (2014) 471–477, http://dx.doi.org/10.1016/j.electacta.2014.04.107.
[44] T. Zhu, J. Zhou, Z. Li, S. Li, W. Si, S. Zhuo, Hierarchical porous and N-doped carbon nanotubes derived from polyaniline for electrode materials in supercapacitors, J. Mater. Chem. A 2 (2014) 12545, http://dx.doi.org/10.1039/C4TA01465K.
[45] J.W.F. To, Z. Chen, H. Yao, J. He, K. Kim, H.-H. Chou, et al., Ultrahigh surface area three-dimensional porous graphitic carbon from Conjugated polymeric molecular framework, ACS Cent. Sci. 1 (2015), http://dx.doi.org/10.1021/acscentsci.5b00149, 150518113247004.
[46] L. Sun, L. Wang, C. Tian, T. Tan, Y. Xie, K. Shi, et al., Nitrogen-doped graphene with high nitrogen level via a one-step hydrothermal reaction of graphene oxide with urea for superior capacitive energy storage, RSC Adv. 2 (2012) 4498, http://dx.doi.org/10.1039/c2ra01367c.
[47] E.J. Jelmy, S. Ramakrishnan, S. Devanathan, M. Rangarajan, N.K. Kothurkar, Optimization of the conductivity and yield of chemically synthesized polyaniline using a design of experiments, J. Appl. Polym. Sci. 130 (2013) 1047–1057, http://dx.doi.org/10.1002/app.39268.
[48] S. Shreepathi, Dodecylbenzenesulfonic Acid: a Surfactant and Dopant for the Synthesis of Processable Polyaniline and its Copolymers, Chemnitz University of Technology, PhD thesis, 2006.
[49] T. Del Castillo-Castro, M.M. Castillo-Ortega, I. Villarreal, F. Brown, H. Grijalva, M. Pérez-Tello, et al., Synthesis and characterization of composites of DBSA-doped polyaniline and polystyrene-based ionomers, Compos. Part A Appl. Sci. Manuf. 38 (2007) 639–645, http://dx.doi.org/10.1016/j.compositesa.2006.02.001.
[50] C.S. Stan, M. Popa, M. Olariu, M.S. Secula, Synthesis and characterization of PSSA-polyaniline composite with an enhanced processability in thin films, Open Chem. 13 (2015) 467–476, http://dx.doi.org/10.1515/chem-2015-0057.
[51] A. John, P.J.P. Yadav, S. Palaniappan, Clean synthesis of 1,8-dioxo-dodecahydroxanthene derivatives catalyzed by polyaniline-p-toluenesulfonate salt in aqueous media, J. Mol. Catal. A Chem. 248 (2006) 121–125, http://dx.doi.org/10.1016/j.molcata.2005.12.017.
[52] A.P. Hussain, A. Kumar, Electrochemical synthesis and characterization of chloride doped polyaniline, Bull. Mater. Sci. 20 (2003) 329–344, http://dx.doi.org/10.1007/BF02707455.
[53] R.C. Rathod, V.K. Didolkar, S.S. Umare, B.H. Shambharkar, Synthesis of processable polyaniline and its anticorrosion performance on 316LN stainless steel, Trans. Indian Inst. Met. 64 (2011) 431–438, http://dx.doi.org/10.1007/s12666-011-0099-0.
[54] G. Neetika, D. Kumar, S.K. Tomar, Thermal behaviour of chemically synthesized polyanilines/polystyrene sulphonic acid composites, Int. J. Mater. Chem. 2 (2012) 79–85, http://dx.doi.org/10.5923/j.ijmc.20120202.07.
[55] R.C. Petterson, U. Grzeskowiak, L.H. Jules, N-halogen compounds. II. 1,2 the N—Cl stretching band in some N-Chloroamides. The structure of trichloroisocyanuric acid, J. Org. Chem. 25 (1960) 1595–1598, http://dx.doi.org/10.1021/jo01079a030.
[56] Z. Chen, Y. Sun, Applied Chemistry N -halamine-based Antimicrobial Additives for Polymers: Preparation, Characterization, and Antimicrobial Activity, 2006, pp. 2634–2640, http://dx.doi.org/10.1021/ie060088a.
[57] S. Sinha, S. Bhadra, D. Khastgir, Effects of dopant type on the properties of polyaniline, Polym. Polym. Compos 21 (2013) 449–456, http://dx.doi.org/10.1002/app.
[58] C.T. Hsieh, H. Teng, Influence of oxygen treatment on electric double-layer capacitance of activated carbon fabrics, Carbon N. Y. 40 (2002) 667–674, http://dx.doi.org/10.1016/S0008-6223(01)00182-8.
[59] X. Gao, A. Omosebi, J. Landon, K. Liu, Surface charge enhanced carbon electrodes for stable and efficient capacitive deionization using inverted adsorption–desorption behavior, Energy Environ. Sci. 8 (2015) 897, http://dx.doi.org/10.1039/c4ee03172e.
[60] L. Wei, G. Yushin, Nanostructured activated carbons from natural precursors for electrical double layer capacitors, Nano Energy 1 (2012) 552–565, http://dx.doi.org/10.1016/j.nanoen.2012.05.002.
[61] J.J. Lado, R.L. Zornitta, F.A. Calvi, M.I. Tejedor-Tejedor, M.A. Anderson, L.A.M. Ruotolo, Study of sugar cane bagasse fly ash as electrode material for capacitive deionization, J. Anal. Appl. Pyrolysis 120 (2016) 389–398, http://dx.doi.org/10.1016/j.jaap.2016.06.009.
[62] Y. Li, I. Hussain, J. Qi, C. Liu, J. Li, J. Shen, et al., N-doped hierarchical porous carbon derived from hypercrosslinked diblock copolymer for capacitive deionization, Sep. Purif. Technol. 165 (2016) 190–198, http://dx.doi.org/10.1016/j.seppur.2016.04.007.
[63] K.S.W. Sing, Reporting physisorption data for gas/solid systems with special reference to the determination of surface area and porosity, Pure Appl. Chem. 54 (1982) 2201–2218, http://dx.doi.org/10.1351/pac198557040603.
[64] M. Aslan, M. Zeiger, N. Jackel, I. Grobelsek, D. Weingarth, V. Presser, Improved capacitive deionization performance of mixed hydrophobic / hydrophilic activated carbon electrodes, J. Phys. Condens. Matter 28 (2016) 114003, http://dx.doi.org/10.1088/0953-8984/28/11/114003.
[65] Y. Qiu, J. Yu, G. Fang, H. Shi, X. Zhou, X. Bai, Synthesis of carbon / carbon core / shell nanotubes with a high specific surface area, Society (2009) 61–68.
[66] E. Frackowiak, Carbon Materials for the Electrochemical Storage of Energy in Capacitors, vol. 39, 2001, pp. 937–950.
[67] G. Rasines, P. Lavela, C. Macías, M.C. Zafra, J.L. Tirado, J.B. Parra, et al., N-doped monolithic carbon aerogel electrodes with optimized features for the electrosorption of ions, Carbon N. Y. 83 (2015) 262–274, http://dx.doi.org/10.1016/j.carbon.2014.11.015.
[68] S. Zhao, T. Yan, H. Wang, G. Chen, L. Huang, J. Zhang, et al., High capacity and high rate capability of nitrogen-doped porous hollow carbon spheres for capacitive deionization, Appl. Surf. Sci. 369 (2016) 460–469, http://dx.doi.org/10.1016/j.apsusc.2016.02.085.
[69] B.M. Asquith, J. Meier-Haack, B.P. Ladewig, Poly(arylene ether sulfone) copolymers as binders for capacitive deionization activated carbon electrodes, Chem. Eng. Res. Des. 104 (2015) 81–91, http://dx.doi.org/10.1016/j.cherd.2015.07.020.
[70] A.J. Bard, L.R. Faulkner, Electrochemical Methods Fundamental and Applications, 2001, http://dx.doi.org/10.1038/nprot.2009.120.Multi-stage.
[71] S. Xiong, F. Yang, H. Jiang, J. Ma, X. Lu, Covalently bonded polyaniline/fullerene hybrids with coral-like morphology for high-performance supercapacitor, Electrochim. Acta 85 (2012) 235–242, http://dx.doi.org/10.1016/j.electacta.2012.08.056.
[72] R. Kötz, M. Carlen, Principles and applications of electrochemical capacitors, Electrochim. Acta 45 (2000) 2483–2498, http://dx.doi.org/10.1016/S0013-4686(00)00354-6.
[73] B. Hirschorn, M.E. Orazem, B. Tribollet, V. Vivier, I. Frateur, M. Musiani, Determination of effective capacitance and film thickness from constant-phase-element parameters, Electrochim. Acta 55 (2010) 6218–6227, http://dx.doi.org/10.1016/j.electacta.2009.10.065.
[74] C.-W. Huang, H. Teng, Influence of carbon nanotube grafting on the impedance behavior of activated carbon capacitors, J. Electrochem. Soc. 155 (2008) A739, http://dx.doi.org/10.1149/1.2965503.
[75] J.B. Zang, Y.H. Wang, H. Huang, W.Q. Liu, Electrochemical characteristics of boron doped polycrystalline diamond electrode sintered by high pressure and high temperature, J. Appl. Electrochem 39 (2009) 1545–1551, http://dx.doi.org/10.1007/s10800-009-9838-x.
[76] C.-M. Chen, Surface Chemistry and Macroscopic Assembly of Graphene for Application in Energy Storage, 2015, http://dx.doi.org/10.1007/978-3-642-35133-4.
[77] G. Xu, C. Zheng, Q. Zhang, J. Huang, M. Zhao, J. Nie, et al., Binder-free activated carbon/carbon nanotube paper electrodes for use in supercapacitors, Nano Res. 4 (2011) 870–881, http://dx.doi.org/10.1007/s12274-011-0143-8.
[78] N.H. Basri, M. Deraman, M. Suleman, N.S.M. Nor, B.N.M. Dolah, M.I. Sahri, et al., Energy and power of supercapacitor using carbon electrode deposited with nanoparticles nickel oxide, Int. J. Electrochem. Sci. 11 (2016) 95–110.
[79] J.H. Choi, Fabrication of a carbon electrode using activated carbon powder and application to the capacitive deionization process, Sep. Purif. Technol. 70 (2010) 362–366, http://dx.doi.org/10.1016/j.seppur.2009.10.023.
[80] K. Yang, T. Ying, S. Yiacoumi, C. Tsouris, Electrosorption of Ions from Aqueous Solutions by Carbon Aerogel: an Electrical Double-layer Model, 2001, pp. 1961–1969.
[81] D. He, C.E. Wong, W. Tang, P. Kovalsky, T. David Waite, Faradaic reactions in water desalination by batch-mode capacitive deionization, Environ. Sci. Technol. Lett. 3 (2016) 222–226, http://dx.doi.org/10.1021/acs.estlett.6b00124.
[82] T. Kim, J. Yu, C. Kim, J. Yoon, Hydrogen peroxide generation in flow-mode capacitive deionization, J. Electroanal. Chem. 776 (2016) 101–104, http://dx.doi.org/10.1016/j.jelechem.2016.07.001.
[83] F. Duan, X. Du, Y. Li, H. Cao, Y. Zhang, Desalination stability of capacitive deionization using ordered mesoporous carbon: effect of oxygen-containing surface groups and pore properties, Desalination 376 (2015) 17–24, http://dx.doi.org/10.1016/j.desal.2015.08.009.
[84] I. Cohen, E. Avraham, Y. Bouhadana, A. Soffer, D. Aurbach, Long term stability of capacitive de-ionization processes for water desalination: the challenge of positive electrodes corrosion, Electrochim. Acta 106 (2013) 91–100, http://dx.doi.org/10.1016/j.electacta.2013.05.029.
[85] B. Shapira, E. Avraham, D. Aurbach, Side reactions in capacitive deionization (CDI) processes: the role of oxygen reduction, Electrochim. Acta 220 (2016) 285–295, http://dx.doi.org/10.1016/j.electacta.2016.10.127.
[86] J.J. Lado, R.E. Pérez-Roa, J.J. Wouters, M.I. Tejedor-Tejedor, C. Federspill, M.A. Anderson, Continuous cycling of an asymmetric capacitive deionization system: an evaluation of the electrode performance and stability, J. Environ. Chem. Eng. 3 (2015) 2358–2367, http://dx.doi.org/10.1016/j.jece.2015.08.025.
[87] J.J. Lado, R.E. Pérez-Roa, J.J. Wouters, M. Isabel Tejedor-Tejedor, M.A. Anderson, Evaluation of operational parameters for a capacitive deionization reactor employing asymmetric electrodes, Sep. Purif. Technol. 133 (2014) 236–245, http://dx.doi.org/10.1016/j.seppur.2014.07.004.
[88] P. Hojati-Talemi, L. Zou, M. Fabretto, R.D. Short, Using oxygen plasma treatment to improve the performance of electrodes for capacitive water deionization, Electrochim. Acta 106 (2013) 494–499, http://dx.doi.org/10.1016/j.electacta.2013.05.119.
[89] T. Kim, J. Yoon, CDI ragone plot as a functional tool to evaluate desalination performance in capacitive deionization, Rsc Adv. 5 (2015) 1456–1461, http://

dx.doi.org/10.1039/c4ra11257a.
[90] A. Yoshida, I. Tanahashi, A. Nishino, Effect of concentration of surface acidic functional groups on electric double-layer properties of activated carbon fibers, Carbon N. Y. 28 (1990) 611–615, http://dx.doi.org/10.1016/0008-6223(90)90062-4.
[91] A. Hemmatifar, J.W. Palko, M. Stadermann, J.G. Santiago, Energy breakdown in capacitive deionization, Water Res. 104 (2016) 303–311, http://dx.doi.org/10.1016/j.watres.2016.08.020.
[92] R. Zhao, P.M. Biesheuvel, A. van der Wal, Energy consumption and constant current operation in membrane capacitive deionization, Energy Environ. Sci. 5 (2012) 9520, http://dx.doi.org/10.1039/c2ee21737f.
[93] Y. Qu, P.G. Campbell, L. Gu, J.M. Knipe, E. Dzenitis, J.G. Santiago, M. Stadermann, Energy consumption analysis of constant voltage and constant current operations in capacitive deionization, Desalination 400 (2016) 18–24, http://dx.doi.org/10.1016/j.desal.2016.09.014.
[94] T. Kim, J. Yoon, Relationship between capacitance of activated carbon composite electrodes measured at a low electrolyte concentration and their desalination performance in capacitive deionization, J. Electroanal. Chem. 704 (2013) 169–174, http://dx.doi.org/10.1016/j.jelechem.2013.07.003.
[95] Y. Liu, T. Chen, T. Lu, Z. Sun, D.H.C. Chua, L. Pan, Nitrogen-doped porous carbon spheres for highly efficient capacitive deionization, Electrochim. Acta 158 (2015) 403–409, http://dx.doi.org/10.1016/j.electacta.2015.01.179.
[96] X. Xu, Z. Sun, D.H.C. Chua, L. Pan, Novel nitrogen doped graphene sponge with ultrahigh capacitive deionization performance, Sci. Rep. 5 (2015) 11225, http://dx.doi.org/10.1038/srep11225.
[97] X. Xu, L. Pan, Y. Liu, T. Lu, Z. Sun, D.H.C. Chua, Facile synthesis of novel graphene sponge for high performance capacitive deionization, Sci. Rep. 5 (2015) 8458, http://dx.doi.org/10.1038/srep08458.
[98] W. Shi, H. Li, X. Cao, Z.Y. Leong, J. Zhang, T. Chen, et al., Ultrahigh performance of novel capacitive deionization electrodes based on A three-dimensional graphene architecture with nanopores, Sci. Rep. 6 (2016) 18966, http://dx.doi.org/10.1038/srep18966.